Published in ApJ, 715, 18

Molecular outflows within the filamentary infrared dark cloud G34.43+0.24

P. Sanhueza[1], G. Garay, L. Bronfman, D. Mardones and J. May

Departamento de Astronomía, Universidad de Chile, Casilla 36-D, Santiago, Chile

and

M. Saito

National Astronomical Observatory of Japan, 2-21-1 Osawa, Mitaka, Tokyo 181-8588, Japan

ABSTRACT

We present molecular line observations, made with angular resolutions of $\sim 20''$, toward the filamentary infrared dark cloud G34.43+0.24 using the APEX [CO($3 \rightarrow 2$), ^{13}CO($3 \rightarrow 2$), C^{18}O($3 \rightarrow 2$) and CS($7 \rightarrow 6$) transitions], Nobeyama 45 m [CS($2 \rightarrow 1$), SiO($2 \rightarrow 1$), C^{34}S($2 \rightarrow 1$), HCO$^+$($1 \rightarrow 0$), H^{13}CO$^+$($1 \rightarrow 0$) and CH$_3$OH($2 \rightarrow 1$) transitions] , and SEST [CS($2 \rightarrow 1$) and C^{18}O($2 \rightarrow 1$) transitions] telescopes. We find that the spatial distribution of the molecular emission is similar to that of the dust continuum emission observed with $11''$ resolution (Rathborne et al. 2005) showing a filamentary structure and four cores. The cores have local thermodynamic equilibrium masses ranging from 3.3×10^2 – 1.5×10^3 M$_\odot$ and virial masses from 1.1×10^3 – 1.5×10^3 M$_\odot$, molecular hydrogen densities between 1.8×10^4 and 3.9×10^5 cm^{-3}, and column densities $> 2.0 \times 10^{22}$ cm^{-2}; values characteristics of massive star forming cores. The ^{13}CO($3 \rightarrow 2$) profile observed toward the most massive core reveals a blue profile indicating that the core is undergoing large–scale inward motion with an average infall velocity of 1.3 km s^{-1} and a mass infall rate of 1.8×10^{-3} M$_\odot$ yr^{-1}. We report the discovery of a molecular outflow toward the northernmost core thought to be in a very early stage of evolution. We also detect the presence of high velocity gas toward

[1]Current address: Institute for Astrophysical Research, Boston University, Boston, MA 02215, USA; patricio@bu.edu

each of the other three cores, giving support to the hypothesis that the excess 4.5 μm emission ("green fuzzies") detected toward these cores is due to shocked gas. The molecular outflows are massive and energetic, with masses ranging from 25 – 80 $M_\odot$, momentum 2.3 – 6.9 $\times$ 10^2 $M_\odot$ km s^{-1}, and kinetic energies 1.1 – 3.6 $\times$ 10^3 $M_\odot$ km^2 s^{-2}; indicating that they are driven by luminous, high-mass young stellar objects.

Subject headings: ISM: clouds — ISM: individual objects (G34.43+0.24) — ISM: jets and outflows — ISM: molecules — stars: formation

1. Introduction

Infrared dark clouds (IRDCs) are cold (<25 K), massive ($\sim10^2$ – 10^4 $M_\odot$), and dense (>10^5 cm^{-3}) molecular clouds with high column densities ($\sim10^{23}$–10^{25} cm^{-2}) seen as a dark silhouette against the bright mid–infrared background emission (Perault et al. 1996; Egan et al. 1998; Carey et al. 1998, 2000; Hennebelle et al. 2001; Simon et al. 2006a, 2006b). A wealth of recent observations show that IRDCs are the sites of high-mass stars and star cluster formation (Rathborne et al. 2006, 2007; Pillai et al. 2006; Jackson et al. 2008; Chambers et al. 2009). Dust continuum observations reveal that IRDCs harbor compact cold cores with typical masses of $\sim$120 $M_\odot$ and sizes <0.5 pc (Rathborne et al. 2006). The masses and sizes of the IRDC cores are similar to those of the massive hot cores (e.g., Garay & Lizano 1999), but IRDC cores are much colder. Recently, Chambers et al. (2009) investigated a sample of 190 cores found toward 38 IRDCs by Rathborne et al. (2006), and classified them as "active" if they are associated with enhanced 4.5 μm emission, the so-called green fuzzies, and an embedded 24 μm source; and "quiescent" if they contain neither of these indicators. They found 37 active cores and 69 quiescent cores. Further, active cores are usually associated with bright (>1 Jy) methanol and water masers (Pillai et al 2006; Wang et al. 2006; Chambers et al. 2009), and have high bolometric luminosities, indicating that they are forming high–mass stars (M > 8 $M_\odot$) stars. The quiescent cores are the most likely candidates for high–mass starless cores.

G34.43+0.24 is an IRDC with a filamentary morphology, extending by $\sim9'$ from north to south in equatorial projection (9.7 pc at the source distance of 3.7 kpc; Faúndez et al. 2004; Simon et al. 2006b). This IRDC is in the list of Rathborne et al. (2006) and Chambers et al. (2009). It is located roughly $11'$ north of the ultra-compact (UC) H II complex G34.26+0.15 (Molinari et al. 1996). Molecular line observations toward this cloud were first reported by Miralles et al. (1994), who from ammonia observations with $1.5'$ resolution found an elongated structure in the N-S direction with a total mass of 1000 $M_\odot$. Near the center of

the filament lies the IRAS point source 18507+0121 which has a luminosity of 3.4×10^4 $L_\odot$.

Bronfman et al. (1996) detected toward IRAS 18507+0121 strong CS($2 \rightarrow 1$) emission with broad line wings, indicating it is associated with a dense massive star forming region. Ramesh et al. (1997) observed the IRAS source in the $HCO^+(1 \rightarrow 0)$, $H^{13}CO^+(1 \rightarrow 0)$, CS($2 \rightarrow 1$) and $C^{34}S(2 \rightarrow 1)$ molecular lines, with angular resolutions of $\sim$16″, modeling the observed line profiles as due to emission from a collapsing hot core that is hidden behind a cold and dense envelope. From observations of 3 mm continuum and $H^{13}CO^+$ line emissions, with $\sim$5″ angular resolution, Shepherd et al. (2004) detected two compact molecular cores, separated by 40″, toward the center of the filament. Millimeter continuum observations revealed the presence of four dust cores (Faúndez et al. 2004; Garay et al. 2004; Rathborne et al. 2005), labeled by the latter authors as MM1, MM2, MM3, and MM4. The MM1 dust core, which corresponds to the northern compact molecular core of Shepherd et al. (2004), contains a deeply embedded luminous object surrounded by several hundred solar masses of warm gas and dust. Based on the weak 6 cm continuum emission and the lack of detection at NIR wavelenghts, Shepherd et al. (2004) suggested that the embedded object appears to be a massive B2 protostar in an early stage of evolution. The MM2 dust core, which corresponds to the southern compact molecular core of Shepherd et al. (2004), is associated with IRAS 18507+0121; with a NIR cluster of young stars with a central B0.5 star (Shepherd et al. 2004); with an UC H II region (Miralles et al. 1994; Molinari et al. 1998); with a variable H_2O maser (Miralles et al. 1994); and with CH_3OH maser emission (Szymczak et al. 2000). The MM3 dust core is located close to the northern edge of the filament, $\sim$3.5′ north of MM2. Garay et al. (2004) suggested that MM3 corresponds to a massive and dense cold core that will eventually collapse to form a high-mass star. The MM4 core is located $\sim$30″ south of MM2 (Rathborne et al. 2005). Table 1 lists the measured 1.2 mm dust continuum emission properties as measured by Rathborne et al. (2006). Rathborne et al. (2005) and Chambers et al (2009) reported an excess 4.5 μm emission toward MM1, MM3, and MM4 cores, which could be produced by either ionized gas and/or shocked gas and acts therefore as a signature of current star formation (MM2 is classified by the last authors as a "red" core, namely with bright 8 μm emission). They also showed that the four MM cores are associated with 24 μm point sources (emission from warm dust), which is an indicator of accretion onto an embedded protostar. Water maser emission, a well–known tracer of low–mass and high–mass star formation, has been detected toward all four MM cores (Wang et al. 2006; Chambers et al. 2009). Chambers et al. (2009) detected Class I CH_3OH masers, another well–know signpost of star formation toward MM1, MM2, and MM3 cores. Rathborne et al. (2006) identified nine 1.2 mm continuum cores with masses ranging from 80 to 1300 $M_\odot$ toward G34.43+0.24.

Shepherd et al. (2007) observed the central region of the filament, encompassing

the MM1 and MM2 cores, at millimeter wavelengths, in CO($1 \rightarrow 0$), ^{13}CO($1 \rightarrow 0$), and C^{18}O($1 \rightarrow 0$) at $\sim 4''$ angular resolution and at near infrared wavelengths with the *Spitzer* Space Telescope. They discovered five massive outflows, three of them associated with the MM2 core and the remaining two associated with the MM1 core. From the *Spitzer* data they identified 31 young stellar objects in the filament, with a combined mass of $\sim$127 M$_\odot$, and additional 22 sources that they believe could be cluster members based on the presence of strong 24 μm emission. Cortes et al. (2008) observed MM1 and MM2 in polarized thermal dust emission at 3 mm and CO($1 \rightarrow 0$) line emission with BIMA array. Their results suggest that there is a magnetic field othogonal to the axis formed by the MM1 and MM2 cores. Recently, Rathborne et al. (2008) carried out high angular submillimeter observations toward the MM1 core using the Submillimeter Array. They determined, using continuum emission images, that MM1 remains unresolved with a size of $\sim$0.03 pc and a mass of 29 M$_\odot$. Their molecular line spectrum shows the presence of several complex molecules, suggesting that MM1 is a hot core. They also found an extended ^{13}CO($3 \rightarrow 2$) structure which may be evidence of a rotating envelope surrounding the central high–mass star, perpendicular to one of the outflows that Shepherd et al. (2007) detected toward MM1.

In this work we report observations of 11 molecular transitions using the APEX 12-m, SEST 15-m, and Nobeyama 45-m telescopes toward the G34.43+0.24 cloud. Since different molecular species trace different density and kinematics regimes, the capability of observing multiple spectral lines is particularly advantageous to determine the morphology and kinematics of star forming cores. Due to the high abundance of CO, the CO($3 \rightarrow 2$) line is an ideal tracer of the low intensity, high–velocity wing emission. The ^{13}CO($3 \rightarrow 2$) line, being more optically thin than CO($3 \rightarrow 2$), traces, in addition to the ambient gas, the low–velocity gas of the molecular outflow. The SiO($2 \rightarrow 1$) line is usually associated with the presence of outflows since its abundance is highly enhanced by shocks. Methanol transitions are usually used as tracers of dense gas, temperature probes and tracers of shocks, since this molecule is evaporated from grain mantles. The HCO$^+$($1 \rightarrow 0$) and CS($2 \rightarrow 1$) lines are high–density tracers and thus are good probes of the dense envelopes surrounding protostars. The C^{18}O($3 \rightarrow 2$), C^{18}O($2 \rightarrow 1$), H^{13}CO$^+$($1 \rightarrow 0$), CS($7 \rightarrow 6$) and C^{34}S($2 \rightarrow 1$) molecular transitions probe the inner regions of the cores. The last two species are weakly influenced by infall and outflow motions, and are used as reference to estimate the central ambient cloud velocity.

The main goals of these multi–line observations are to determine the morphology and kinematics of the gas within the molecular cores in the G34.43+0.24 filamentary IRDC, in particular to investigate the presence of outflowing gas, in order to increase our knowledge of the evolutionary state of the cores and to achieve a better understanding of the overall process of massive star formation along the filament. This is the first survey of several

molecular lines mapping portions and the whole cloud. It gives us, for the first time, a comprehensive view of the molecular gas distribution at the scale of parsecs.

2. Observations

The observations were made using the 12-m APEX[1] telescope, the 15-m SEST telescope, both located in Chile, and the 45-m telescope of the Nobeyama Radio Observatory (NRO) located in Japan. The molecules, transitions, frequencies and observing parameters are listed in Table 2.

2.1. APEX Telescope

With the APEX telescope we observed the CO($3 \rightarrow 2$), ^{13}CO($3 \rightarrow 2$), C^{18}O($3 \rightarrow 2$) and CS($7 \rightarrow 6$) lines. The observations were carried out during three epochs: 2005 July, 2005 October, and 2006 May-July. The telescope beam size at the frequency of the observed lines ranged from 17 to 19″ (FWHM). We used the heterodyne receiver (APEX-2a), which provided a channel separation of 122 kHz and a total bandwidth of 1 GHz with 8192 spectral channels.

In CO($3 \rightarrow 2$) and ^{13}CO($3 \rightarrow 2$), we mapped the emission within a 100″×680″ region which cover a spatial extent similar to that exhibited by the 1.2 mm dust continuum emission map (see Garay et al. 2004). The spacing between adjacent points on a regular grid was 20″ and the position-switching mode was used. The on-source integration time per map position was typically ∼40 s in both molecules. System temperatures were in the range 110-340 K in CO($3 \rightarrow 2$) and 200-300 K in ^{13}CO($3 \rightarrow 2$), resulting in an rms noise per channel, in antenna temperature, of typically 0.27 K and 0.37 K, respectively. In C^{18}O($3 \rightarrow 2$) we mapped the emission within a 80″×100″ zone, covering the central region of the filament also known as the IRAS 18507+0121 region. System temperatures were typically ∼190 K. The on-source integration time per map position was ∼50 s resulting an rms noise per channel of typically 0.29 K in antenna temperature. In CS($7 \rightarrow 6$) we mapped the emission within a 40″×120″ region. System temperatures were typically ∼200 K. On-source integration time was ∼80 s resulting an rms noise per channel of typically 0.18 K in antenna temperature.

The molecular line data were reduced according to the standard procedure using CLASS,

[1]Atacama Pathfinder EXperiment. APEX is a collaboration between the Max-Planck-Institut fur Radioastronomie, the European Southern Observatory and the Onsala Space Observatory.

a GILDAS working group software.

2.2. NRO 45 m Telescope

With the NRO 45 m telescope we observed the CS($2 \rightarrow 1$), SiO($2 \rightarrow 1$), $C^{34}S(2 \rightarrow 1)$, $HCO^+(1 \rightarrow 0)$, $H^{13}CO^+(1 \rightarrow 0)$ and $CH_3OH(2 \rightarrow 1)$ lines toward the central region of the filament. The observations were undertaken during 1996 February-April. The telescope beam size at the frequencies of the observed lines is 15-18″. We used an acousto-optical spectrometer with 37 kHz resolution covering a total bandwidth of 40 MHz.

The emission was mapped in all lines within a 80″×140″ region. The spacing between adjacent points on a regular grid was 20″, using the position-switching mode. System temperatures were in the range between 160 and 390 K. On-source integration times per map position ranged from 300 to 600 s resulting in rms noise of typically 0.08 K per channel in antenna temperature in all lines. First–order polynomials were fitted in order to estimate and remove the baselines. Part of this data were used by Ramesh, Bronfman & Deguchi (1997) to model the kinematics at the peak position of IRAS 18507+0121.

2.3. SEST Telescope

With the SEST telescope we observed the CS($2 \rightarrow 1$) and $C^{18}O(2 \rightarrow 1)$ lines toward the northern part of the filament (MM3 core). The telescope beam size is 24″ at the frequency of the $C^{18}O(2 \rightarrow 1)$ line and 51″ at the frequency of the CS($2 \rightarrow 1$) line. The observations were carried out in 2003 March. We used the high-resolution acousto-optical spectrometers, which provided a channel separation of 43 kHz and a total bandwidth of 43 MHz. We observed, with 30″ spacing between adjacent points on a regular grid, 25 positions within a 150″×150″ region. The on-source integration times per map position were typically ∼130 s for CS and ∼70 s for $C^{18}O$. System temperatures were in the range 230-270 K for CS and 400-540 K for $C^{18}O$, resulting in an rms noise, in antenna temperature, of typically 0.07 K and 0.18 K per channel, respectively.

3. Results

3.1. Filament and Dense Cores

Figure 1 shows the $^{13}CO(3 \rightarrow 2)$ spectra observed with APEX along the whole filamentary structure detected in the 1.2 mm dust continuum observations of Garay et al. (2004; see their Figure 4). Emission in the $^{13}CO(3 \rightarrow 2)$ line was detected across the whole mapped region.

Figure 2 shows contour maps of the velocity integrated ambient gas emission (velocity range from 52.9 to 61.1 km s^{-1}, determined by inspection of the line profiles) in the $^{13}CO(3 \rightarrow 2)$, $CS(7 \rightarrow 6)$, $CS(2 \rightarrow 1)$, $SiO(2 \rightarrow 1)$, $H^{13}CO^{+}(1 \rightarrow 0)$ and $C^{18}O(3 \rightarrow 2)$ lines observed toward the central $\sim 1.5' \times 3'$ region of the filament. The maps are overlaid on a grey scale image of the 1.2 mm dust continuum emission observed with SIMBA/SEST by Garay et al. (2004). We find that the morphology of the molecular line emission resembles that of the dust continuum emission, showing two components: a northern component associated with the MM1 core and a southern component associated with the MM2 dust core. There are, however, some differences in the morphology of the emission in the different molecular lines. These are likely due to chemistry and/or optical depth effects and/or differences in the regimes of density and temperature traced by the different lines. In particular, the emission in the $CS(7 \rightarrow 6)$ line is less extended than in the other transitions and runs nearly parallel to the north-south direction.

Figure 3 presents contour maps of the velocity integrated ambient gas emission (velocity range from 55.8 to 60.6 km s^{-1}) in three methanol lines [$CH_3OH(2_0 \rightarrow 1_0)$ A+, $CH_3OH(2_{-1} \rightarrow 1_{-1})$ E, $CH_3OH(2_0 \rightarrow 1_0)$ E] observed toward the central region of G34.43+0.24. The maps are overlaid on a gray scale image of the 1.2 mm dust continuum emission observed with SIMBA/SEST. The morphology of the emission in the three methanol lines is all similar. They are, however, different from the morphology exhibited by the dust continuum emission and the rest of the molecular lines. The methanol peaks do not coincide with the dust peaks, on the contrary they seem to be slightly anticorrelated. This could be due to depletion of methanol within the central regions of the dust cores.

Figure 4 shows contour maps of velocity-integrated ambient gas emission (velocity range from 56.1 to 61.5 km s^{-1}) in the $^{13}CO(3 \rightarrow 2)$, $CS(2 \rightarrow 1)$ and $C^{18}O(2 \rightarrow 1)$ lines observed toward the MM3 core, overlaid on a gray scale image of the 1.2 mm dust continuum emission. Whereas the morphology of the emission in the $^{13}CO(3 \rightarrow 2)$ line is similar to that of the dust continuum emission, that in the $C^{18}O(2 \rightarrow 1)$ line is somewhat different, showing a peak that is displaced from the peak of the dust emission.

Table 3 gives the observed parameters of the molecular cores. The angular sizes, determined from the contour maps, correspond to the observed semi-major and semi-minor axes. The line center velocity, line width and velocity-integrated brightness temperature were determined from Gaussian fits to the composite spectra of the ambient cloud emission within each core. The cores are assumed to be at a distance of 3.7 kpc, which corresponds to the kinematical distance of IRAS 18507+0121 reported by Faúndez et al. (2004) and the kinematical distance of the IRDC given by Simon et al. (2006b).

3.2. Spectra Observed Toward the Dense Cores

There are notable differences between the line profiles observed in different molecular species, for different positions. In what follows we describe the spectra observed toward three selected positions (0″, 20″), (20″, -20″) and (40″, 200″) associated with, respectively, the MM1, MM2 and MM3 dust peaks.

Figure 5 shows the spectra observed toward the (0″, 20″) position, which corresponds to the MM1 core. The CO($3 \rightarrow 2$) profile shows, in addition to considerable self-absorption, the presence of both blueshifted and redshifted high velocity emission. The strong CO($3 \rightarrow 2$) wing emission at redshifted velocities is also clearly seen in the SiO($2 \rightarrow 1$), CS($2 \rightarrow 1$), and $HCO^+(1 \rightarrow 0)$ spectra.

Figure 6 shows the spectra observed toward the (20″,−20″) position (MM2 core). The CO($3 \rightarrow 2$) profile shows considerable self-absorption, and the presence of high velocity emission at both blueshifted and redshifted velocities. The ^{13}CO($3 \rightarrow 2$) line profile exhibits a strong blueshifted feature, with a peak at the velocity of 55.8 km s^{-1}, and a flat redshifted shoulder. The $C^{18}O(3 \rightarrow 2)$ line shows strong emission toward blueshifted velocities, with a peak at the velocity of 56.1 km s^{-1}, and a skewed profile toward redshifted velocities. A similar profile is seen in the $H^{13}CO^+(1 \rightarrow 0)$ line. The CS($2 \rightarrow 1$) and $HCO^+(1 \rightarrow 0)$ lines show double-peaked profiles; the former exhibits a strong blue peak and a weaker red peak whereas the later shows an opposite asymmetry, namely a strong redshifted peak and a weaker blueshifted peak. The CS($7 \rightarrow 6$) and $C^{34}S(2 \rightarrow 1)$ lines exhibit symmetrical profiles, with peak line center velocites, determined from Gaussian fits, of 58.1 ± 0.1 km s^{-1} and 57.4 ± 0.2 km s^{-1}, respectively.

Ramesh et al. (1997) modeled the observed CS($2 \rightarrow 1$), $C^{34}S(2 \rightarrow 1)$, $HCO^+(1 \rightarrow 0)$ and $H^{13}CO^+(1 \rightarrow 0)$ profiles toward MM2 as being produced by a collapsing hot core hidden behind a cold intervening screen or envelope. We have modeled here the line profiles of $^{13}CO(3 \rightarrow 2)$, $C^{18}O(3 \rightarrow 2)$ and CS($7 \rightarrow 6$) using the simple model of spectral-line profiles

from contracting clouds of Myers et al. (1996). We concluded that the MM2 core is undergoing large-scale inward motions with a infall velocity of $\sim$1.3 km s^{-1} (see section 4.1.2).

Figure 7 shows the spectra observed toward the (40″, 200″) position, which corresponds to the MM3 core. The CO($3 \rightarrow 2$) spectrum shows, in addition to considerable self-absorption, strong blueshifted wing emission up to a velocity of 42.2 km s^{-1}. The ^{13}CO($3 \rightarrow 2$) spectrum exhibits a strong Gaussian line, with a center velocity of 58.5 $\pm$ 0.1 km s^{-1}, and blueshifted wing emission up to a velocity of 53.6 km s^{-1}. These observations strongly indicate the presence of an energy source within the MM3 core. The C^{18}O($2 \rightarrow 1$) and CS($2 \rightarrow 1$) spectra exhibit nearly Gaussian lines profiles with peak line center velocities of 58.9 $\pm$ 0.1 and 58.8 $\pm$ 0.1 km s^{-1}, respectively.

3.3. Molecular Outflows

3.3.1. Central Region

Figure 8 shows position-velocity diagrams of the CO($3 \rightarrow 2$), CS($2 \rightarrow 1$), SiO($2 \rightarrow 1$), and ^{13}CO($3 \rightarrow 2$) emission, toward the central region of G34.43+0.24, along two cuts in the north-south direction passing through the peak position of the MM1 (left panel) and MM2 (right panel) cores. Strikingly seen in this Figure is the presence of high velocity gas associated with the MM1 and MM2 cores, most likely due to molecular outflows emanating from both cores. Particularly notable is the detection of emission in the silicon monoxide line, which is a powerful tracer of the presence of strong shocks. The abundance of SiO molecules is highly enhanced, with respect to ambient abundances, in molecular outflows as a result of destruction of dust grains by shocks, giving rise to the injection into the gas phase of Si atoms and/or Si-bearing species. Once silicon is injected into the gas phase, chemical models based on ion-molecule reactions predict a large abundance of SiO molecules (Turner & Dalgarno 1977; Hartquist et al. 1980).

In the cut passing through the peak of MM1, the most prominent outflow emission is seen redshifted with respect to the ambient gas velocity, extending up to velocities of 80.7 km s^{-1} in CO($3 \rightarrow 2$) and 70.2 km s^{-1} in CS($2 \rightarrow 1$) and SiO($2 \rightarrow 1$). Weak or no outflow emission is detected in the ^{13}CO($3 \rightarrow 2$) line, indicating low optical depths. In the cut passing through the peak of MM2, both blueshifted and redshifted high velocity emission are clearly seen emanating from the MM2 core. In CO($3 \rightarrow 2$) the blueshifted and redshifted emissions extend up to velocities of 42.0 and 74.2 km s^{-1}, respectively. Also seen in this cut is wing emission emanating from the MM1 core as well as from the MM4 core, suggesting that MM4 also contains an outflow.

Maps of the velocity integrated line wing emission, in the CO($3 \rightarrow 2$), SiO($2 \rightarrow 1$) and CS($2 \rightarrow 1$) lines toward the central $1.5' \times 3'$ region of G34.43+0.24, including the MM1, MM2 and MM4 dust cores, are shown in Figure 9. In SiO($2 \rightarrow 1$) and CS($2 \rightarrow 1$), the range of velocity integration of the blueshifted emission (blue contours or solid lines) is $49.0 < v_{lsr} < 52.9$ km s^{-1}, whereas that of the redshifted emission (red contours or dashed lines) is $61.1 < v_{lsr} < 65.2$ km s^{-1}. In CO($3 \rightarrow 2$) the range of velocity integration of the blueshifted and redshifted emissions are, respectively, $42.0 < v_{lsr} < 53.0$ km s^{-1} and $62.0 < v_{lsr} < 74.0$ km s^{-1}. In Fig. 9 we identify two, possibly three, outflows associated with the dust cores within the region considered. The northernmost outflow (labeled O-MM1) is associated with the MM1 core. It is roughly oriented in the NE-SW direction, with the peaks of the redshifted and blueshifted emission being located, respectively, SW and NE of the 3 mm continuum source detected by Shepherd et al. (2004; marked with a star). There is, however, a large spatial overlap between the blueshifted and redshifted emissions.

The outflow associated with the MM2 core, (labeled O-MM2), shows a complex morphology with the blueshifted and redshifted emission exhibiting a considerable spatial overlap. The peak position of the redshifted and blueshifted emissions are located $\sim 7''$ south of the UC HII region (marked with a triangle) and are coincident within the errors. This suggest that the symmetry axis of the outflow is close to the line of sight.

Outflow-MM4 is associated with the MM4 dust core (marked with a square). The blueshifted and redshifted emissions exhibit a large overlap in their spatial distribution, suggesting that the flow is unresolved or that its axis of symmetry is close to the line of sight.

3.3.2. Northern Region

Figure 10 shows position-velocity diagrams of the CO($3 \rightarrow 2$) and ^{13}CO($3 \rightarrow 2$) emission toward the northern region of G34.43+0.24, along a line in the north-south direction passing through the peak position of the MM3 core. Clearly seen in the CO($3 \rightarrow 2$) cut is the presence of wing emission emanating from MM3, with velocities extending up to 42.2 km s^{-1} in the blueshifted side and 69.2 km s^{-1} in the redshifted side. In the ^{13}CO($3 \rightarrow 2$) line the wing emission is barely seen.

Figure 11 shows maps of the integrated line wing emission, in the CO($3 \rightarrow 2$) and ^{13}CO($3 \rightarrow 2$) lines, toward the MM3 core. The range of velocity integration of the blueshifted emission (blue contours) is $41.2 < v_{lsr} < 56.1$ km s^{-1} for CO($3 \rightarrow 2$) and $52.6 < v_{lsr} < 56.1$ km s^{-1} for ^{13}CO($3 \rightarrow 2$); whereas that of the redshifted emission (red contours) is $61.5 <$

$v_{lsr} < 69.4$ km s^{-1} for CO($3 \rightarrow 2$) and $61.5 < v_{lsr} < 63.8$ km s^{-1} for ^{13}CO($3 \rightarrow 2$). In the CO($3 \rightarrow 2$) map, the peak positions of the redshifted and blueshifted wing emissions are located, respectively, NE and SW of the peak position of the millimeter dust core. The red and blue wing emissions exhibit however a considerable overlap in their spatial distribution.

4. Discussion

4.1. Molecular Cores

4.1.1. Physical Parameters

From the observations of the ^{13}CO($3 \rightarrow 2$) and C^{18}O($3 \rightarrow 2$) lines it is possible to estimate the column density and the mass of molecular gas within the central region (MM1 and MM2 cores) as follows. Assuming that the C^{18}O($3 \rightarrow 2$) line is emitted under local thermodynamic equilibrium (LTE) conditions and its emission is optically thin, then the column density is given by (e.g., Bourke et al. 1997)

$$N(\mathrm{C^{18}O}) = 8.084 \times 10^{13} \, \frac{(T_{ex} + 0.88) \exp(15.81/T_{ex})}{1 - \exp(-15.81/T_{ex})} \iint \tau_{18} dv \ , \tag{1}$$

where τ_{18} is the optical depth of the C^{18}O($3 \rightarrow 2$) line, T_{ex} is the excitation temperature, and v is in km s^{-1}. The LTE mass can be obtained from

$$\left(\frac{M_{LTE}}{M_\odot}\right) = 0.565 \left(\frac{\mu_m}{2.72 m_H}\right) \left(\frac{[\mathrm{H_2/C^{18}O}]}{3.8 \times 10^6}\right) \left(\frac{D}{\mathrm{kpc}}\right)^2 \frac{(T_{ex} + 0.88) \exp(15.81/T_{ex})}{1 - \exp(-15.81/T_{ex})} \iint \tau_{18} dv d\Omega \ , \tag{2}$$

where μ_m is the mean molecular mass per H_2 molecule, m_{H} is the mass of a hydrogen atom, D is the source distance, [H_2/C^{18}O] is the H_2 to C^{18}O abundance ratio, and Ω is in arcmin^2. The opacities in the C^{18}O($3 \rightarrow 2$) line are obtained from the ratio of the observed brightness temperatures in the C^{18}O($3 \rightarrow 2$) and ^{13}CO($3 \rightarrow 2$) lines as follows (see Bourke et al. 1997, for derivation)

$$\frac{1 - \exp\left(-\tau_{18}/r\right)}{1 - \exp\left(-\tau_{18}\right)} = \frac{[J_{18}(T_{ex}) - J_{18}(T_{\mathrm{bg}})]}{[J_{13}(T_{ex}) - J_{13}(T_{\mathrm{bg}})]} \frac{T_{\mathrm{mb}}(^{13}\mathrm{CO})}{T_{\mathrm{mb}}(\mathrm{C^{18}O})} \ , \tag{3}$$

where T_{bg} is the background temperature, T_{mb} is the main beam brightness temperature of the line, J is given by (the subscripts "18" and "13" refer to the C^{18}O and ^{13}CO isotopes, respectively)

$$J(T) = \frac{h\nu}{k} \frac{1}{\exp(h\nu/kT) - 1} \ , \tag{4}$$

and, $r = \tau_{18}/\tau_{13}$ is the optical depth ratio

$$\frac{\tau_{18}}{\tau_{13}} = \left[\frac{\mathrm{C^{18}O}}{\mathrm{^{13}CO}}\right] \frac{(kT_{ex}/hB_{13} + 1/3)}{(kT_{ex}/hB_{18} + 1/3)} \frac{\exp(E_{J_{13}}/kT_{ex})}{\exp(E_{J_{18}}/kT_{ex})} \frac{[1 - \exp(-h\nu_{18}/kT_{ex})]}{[1 - \exp(-h\nu_{13}/kT_{ex})]} \ , \tag{5}$$

where B is the rotational constant of the molecule, $E_J = hBJ(J+1)$ is the rotational energy at the lower state, and J is the rotational quantum number. Assuming an [^{13}CO/C^{18}O] abundance ratio of 7.6, we derive average optical depths in C^{18}O($3 \rightarrow 2$) of 0.10 and 0.18 toward the MM1 and MM2 cores, respectively. Using an excitation temperature of 30 K and an [H$_2$/C^{18}O] abundance ratio of 3.8×10^6 (Wilson & Rood 1994) we derive total masses of 330 and 1460 M$_\odot$ for the MM1 and MM2 cores, respectively. The derived core parameters are listed in Table 4.

Masses can also be estimated assuming that the clouds are in virial equilibrium. Neglecting magnetic fields and external forces, the virial mass, M_{vir}, for a spherical cloud of radius R is given by (MacLaren, Richardson & Wolfendale 1988)

$$M_{vir} = B \left(\frac{R}{\mathrm{pc}}\right) \left(\frac{\Delta v}{\mathrm{km\ s^{-1}}}\right)^2 \ M_\odot \ , \tag{6}$$

where Δv is the average line width in km s^{-1}, R in pc, and B is a constant which depends on the density profile of the cloud. Assuming that the cores have uniform densities ($B = 210$) we derive virial masses of 1.1×10^3, 1.5×10^3 and 1.4×10^3 M$_\odot$ for, respectively, the MM1, MM2 and MM3 cores. These values correspond to the geometric mean of the masses determined from the transitions given in Table 5. The molecular hydrogen densities were computed from the mass assuming that the cloud has a spherical morphology and a uniform density.

Table 6 summarizes the core masses determined from different methods and authors. Cols. (2) and (3) give the LTE and the virial masses, respectively, determined in this work; col. (4) gives the LTE mass from Shepherd et al. (2007); and, cols. (5) and (6) give the masses derived from dust continuum observations by Garay et al. (2004) and Rathborne et al. (2006), respectively. In our estimate, if the excitation temperature is 25 or 35 K, the LTE mass is decreased or increased by $\sim$20%, respectively. Given the uncertainties associated with each method – such as in the abundance, excitation temperature, dust temperature, and dust opacity – the agreement is good between the masses determined in this work and the masses determined from dust emission. Differences in the mass obtained by different authors using dust emission are mostly due to different dust temperatures and core sizes used in their calculations. There are, however, discrepancies with the masses determined by Shepherd et al. (2004) from H^{13}CO$^+$($1 \rightarrow 0$) observations, of 4000 and 5000 M$_\odot$ for MM1 and MM2, respectively, and a total cloud mass of 50000 M$_\odot$. We note that Rathborne et al. (2005) estimated from dust emission observations a total cloud mass of 7500 M$_\odot$ assuming

a dust temperature of 30 K. A possible explanation of the larger mass estimate of Shepherd et al. (2004) is that the actual abundance of HCO^+ is probably larger than the adopted one, due to an enhancement produced by the molecular outflows. Moreover, Shepherd et al. (2007) determined, from observations of the $C^{18}O(1 \rightarrow 0)$ line using the OVRO array, masses of 75 and 690 $M_\odot$ for MM1 and MM2, respectively. These values probably correspond to the inner mass of the cores. We note that masses derived from molecular lines might not be tracing all of the emission, and their emission may be optically thick, specially $C^{18}O(1 \rightarrow 0)$. However, the assumption that the $C^{18}O(3 \rightarrow 2)$ is optically thin seems to be adequate and it is supported for the inspection of the line profiles and values obtained for the optical depths.

Optical depths and column densities toward the peak position of the MM1 and MM2 cores are given in Table 7. The $C^{34}S(2 \rightarrow 1)$ and $CS(2 \rightarrow 1)$ values were obtained in an analogous way to that described above for the $C^{18}O(3 \rightarrow 2)$ and $^{13}CO(3 \rightarrow 2)$ lines, adopting a $[CS/C^{34}S]$ abundance ratio of 22.5 and an $[H_2/CS]$ ratio of 1×10^8 (e.g., van der Tak et al. 2000).

4.1.2. MM2: a Collapsing Core

The $^{13}CO(3 \rightarrow 2)$ line emission at the peak position of the MM2 core shows a bright blueshifted peak and a flat redshifted shoulder. Such line shape can be modeled as due to inward motions (Mardones et al. 1997). The blue peak is produced by high excitation gas on the far side of the envelope, while the redshifted peak results from low excitation gas in the near side of the envelope. The self–absorption due to low excitation, low velocity gas in the near side of the envelope gives rise to the central dip (Evans 1999). An estimate of the infall velocity, V_{in}, can be obtained using the two–layer infall model of Myers et al. (1996).

Myers et al. (1996) made a simple analytic model of radiative transfer in order to inspect if the observed spectra show any evidence of infall motions and to provide an estimate of the characteristic V_{in}. They assumed two uniform regions of equal temperature and velocity dispersion σ, whose density and velocity are attenuation-weighted means over the front and rear halves of a centrally condensed, contracting cloud with $n/n_{max} = (r/r_{min})^{-3/2}$ and $V/V_{max} = (r/r_{min})^{-1/2}$. We modeled the profile of the $^{13}CO(3 \rightarrow 2)$, $C^{18}O(3 \rightarrow 2)$ and $CS(7 \rightarrow 6)$ lines toward the MM2 core using their prescription and obtained the following model parameters: the peak optical depth, τ_0; the kinetic temperature, T_k; the infall velocity, V_{in}; and the non–thermal velocity dispersion, $\sigma_{_{NT}}$. Figure 12 shows the observed and the best model line profiles, indicating motions consistent with a "fast" infall, $V_{in} \sim \sigma$. The values derived by the model are shown in the top right corner in the same figure. We note that some of the parameters for each fit are different, for example, the infall velocities are

1.5, 1.3, and 1.0 km s^{-1} for ^{13}CO, C^{18}O, and CS, respectively. This decreasing order is in accord with the level of asymmetry in the lines. The most asymmetric line, a single peak in the blue and a red shoulder, has the largest values of V_{in} (Myers et al. 1996; Fuller et al. 2005). Although the velocity dispersion in the CS line is $\sigma \sim 2V_{in}$, the other two lines have $\sigma \sim V_{in}$ indicating a fast infall. The derived systemic velocities show some scatter, most likely due to the influence of the molecular outflow, which is more intense toward redshifted velocities. If the contribution of the outflow is removed, the blue peak becomes stronger than the red shoulder, and this will have the effect of increasing the derived infall velocity.

Ramesh et al. (1997) modeled the profile of the CS($2 \rightarrow 1$), C^{34}S($2 \rightarrow 1$), HCO$^+$($1 \rightarrow 0$) and H^{13}CO$^+$($1 \rightarrow 0$) lines toward the MM2 core using both the large velocity gradient (LVG) method and the simple model of Myers et al. (1996). For the LVG method they adopted a constant temperature of 22 K (we determined a kinetic temperature of ∼36 K), and found a collapse velocity that varies radially as $8(r/r_0)^{-0.6}$ km s^{-1} with $r_0 = 4.5 \times 10^{16}$ cm. At a radius of $r = 5.5 \times 10^{17}$ cm (equivalent to an angular size of 10″) we get $V_{in} = 1.8$ km s^{-1}. Given the uncertainties associated with each method, the agreement is good with the values determined by us. The infall speed estimated by Ramesh et al. (1997) using the Myers et al. (1996) analytic model is about 1 order of magnitude smaller than the velocities they determine from the LVG analysis; however, since the fit of the Myers model is admittedly not too good, they argue in favor of the larger value, which agrees well with ours here.

The mass infall rate can be estimated assuming $\dot{M} = M_R V_{in}/R$, where M_R is the mass within the radius R and V_{in} is the infall speed at radius R. Using the LTE mass derived at the central position of MM2, of 240 M$_\odot$, an average infall velocity of 1.3 km s^{-1}, and a radius of 5.5×10^{17} cm (corresponding to a 10″angular radius); we obtain a mass infall rate of 1.8×10^{-3} M$_\odot$ yr^{-1}. Such accretion rate is high enough to overcome the radiation pressure of the central star and to form a massive star. Shepherd et al. (2007) identified two likely massive stars (M > 8 M$_\odot$) with the MM2 core, with one of them, located near the projected center of the UC H II region, having a spectral type of B0.5 (Shepherd et al. (2004). Models of massive envelopes accreting onto this kind of young stars require accretion rates of $\dot{M} > 5 \times 10^{-4}$ M$_\odot$ yr^{-1} (Osorio, Lizano & D'Alessio 1999), in agreement with our results.

4.2. Molecular Outflows

To compute physical parameters of the outflowing gas, we followed the standard LTE formalism described in Bourke et al. (1997) using the emission in the CO($3 \rightarrow 2$) line. The main source of error in determining the mass in the outflow arises from the difficulty

in separating the contribution to the outflows of the emission in the velocity range of the ambient cloud. We adopt as velocity boundary between the blue and red wing emission and the ambient emission the values of, respectively, 53.0 and 60.8 km s^{-1} for the MM1 outflow, 51.8 and 60.9 km s^{-1} for the MM2 outflow, and 56.1 and 61.5 km s^{-1} for the MM3 outflow. Another source of error is the possibility that the CO($3 \rightarrow 2$) line might not be optically thin, particularly at low flow velocities. Fortunately, with the available data, we can asses this effect and make corrections.

The mass in the high velocity wings is estimated from the CO(3→2) observations as follows. Assuming that the energy levels of CO are populated according to LTE and that the outflow emission is optically thin, then the total CO column density, N(CO), at each observed position is given by (e.g., Garden et al. 1991)

$$N(\mathrm{CO}) = 7.7 \times 10^{13} \, \frac{(T_{ex} + 0.92) \, \exp(16.60/T_{ex})}{[1 - \exp(-16.60/T_{ex})]} \, \frac{1}{[J(T_{ex}) - J(T_{bg})]} \int T_B(v) dv \ , \qquad (7)$$

where T_{ex} is the excitation temperature of the population in the rotational levels, T_{bg} is the background temperature, T_B is the brightness temperature of the CO(3→2) emission at velocity v, v is measured in km s^{-1}, and J is defined by equation (4). The mass is then computed from the derived column densities as,

$$M = [\mathrm{H_2/CO}] \ \mu_m \ A \ \sum N(\mathrm{CO}) \ , \qquad (8)$$

where μ_m is the mean molecular mass per H_2 molecule, [H_2/CO] is the molecular hydrogen to carbon monoxide abundance ratio, A is the size of the emitting area in an individual position, and the sum is over all the observed positions inside each lobe.

From the observations of the CO($3 \rightarrow 2$) and ^{13}CO($3 \rightarrow 2$) lines it is possible to estimate the opacities of the flowing gas and therefore to assess whether or not the assumption that the CO($3 \rightarrow 2$) wing emission is optically thin is correct. Using expressions (3) and (5) for ^{12}CO and ^{13}CO, assuming T_{ex} = 30 K, and [^{12}CO/^{13}CO] = 50, we find that the average CO($3 \rightarrow 2$) opacities of the blueshifted gas (in the velocity range from 49.5 to 53.0 km s^{-1}) and redshifted gas (in the velocity range from 60.8 to 68.9 km s^{-1}) of the MM1 flow are 3.4 and 2.5, respectively. The given ranges are those in which emission is detected in both lines. For the MM2 outflow we find that the average optical depth of the blueshifted gas (in the velocity range from 47.2 to 51.8 km s^{-1}) and redshifted gas (in the velocity range from 60.9 to 68.7 km s^{-1}) are 5.4 and 4.4, respectively. For the MM3 outflow we find that the average optical depth of the blueshifted gas (velocity range from 52.8 to 56.1 km s^{-1}) and redshifted gas (velocity range from 61.5 to 65.2 km s^{-1}) are 7.1 and 4.2, respectively. These calculations indicate that the CO($3 \rightarrow 2$) emission from the flowing gas, in the given velocity ranges, is moderately optically thick for the three flows. On the other hand, as the

position–velocity diagrams suggested, the ^{13}CO flow emission is optically thin, with optical depths between 0.05 and 0.13.

To correct the mass determined under the optically thin assumption by the opacity effect we divided the CO($3 \rightarrow 2$) wing emission into two regimes, an optically thin regime, in which no ^{13}CO($3 \rightarrow 2$) emission is detected, and an optically thick regime. We assumed an [H_2/CO] abundance ratio of 10^4 (Frerking, Langer & Wilson 1982) and an excitation temperature of the outflowing gas of 30 K. We derived masses in the optically thin regime of the 0.5, 1.1, and 1.6 $M_\odot$ for the blueshifted lobes of MM1 ($38.6 < v_{\rm lsr} < 49.5$ km s^{-1}), MM2 ($35.9 < v_{\rm lsr} < 47.2$ km s^{-1}), and MM3 ($40.1 < v_{\rm lsr} < 52.8$ km s^{-1}), respectively, and masses of 0.7, 0.8, and 0.7 $M_\odot$ for the redshifted lobes of MM1 ($68.9 < v_{\rm lsr} < 74.5$ km s^{-1}), MM2 ($68.7 < v_{\rm lsr} < 74.5$ km s^{-1}), and MM3 ($65.2 < v_{\rm lsr} < 74.3$ km s^{-1}), respectively. In the optically thick regime the mass determined under the optically thin assumption is multiplied by the factor $\tau_{\rm w}/(1 - e^{-\tau_{\rm w}})$, where $\tau_{\rm w}$ is the average CO($3 \rightarrow 2$) optical depth of wing emission in the optically thick velocity range. We derive masses in the optically thick regime, corrected by opacity, of 2.6, 13.6, and 8.5 $M_\odot$ for the blueshifted lobes of MM1 ($49.5 < v_{\rm lsr} < 53.0$ km s^{-1}), MM2 ($47.2 < v_{\rm lsr} < 51.8$ km s^{-1}), and MM3 ($52.8 < v_{\rm lsr} < 56.1$ km s^{-1}), respectively. Similarly, for the redshifted lobes we derived masses of 11.9, 30.8, and 7.3 $M_\odot$ toward MM1 ($60.8 < v_{\rm lsr} < 68.9$ km s^{-1}), MM2 ($60.9 < v_{\rm lsr} < 68.7$ km s^{-1}), and MM3 ($61.5 < v_{\rm lsr} < 65.2$ km s^{-1}), respectively.

To estimate the contribution to the flow mass from the low velocity material emitting in the same velocity range as the ambient cloud gas, we followed the prescription of Margulis & Lada (1985). Using expression (A16) of Bourke et al. (1997),

$$\int_{\rm lobe} \int_{v_b}^{v_r} T_{\rm mb}\, dv\, d\Omega = \int_{\rm lobe} \left(\frac{T^b + T^r}{2} \right) (v_r - v_b)\, d\Omega \ , \tag{9}$$

where T^b, v_b and T^r, v_r are the brightness temperature and velocity at the blue and red velocity boundaries, respectively. We estimated that the hidden flow masses corrected by opacity in the low velocity range within the blueshifted lobes toward MM1, MM2 and MM3 are 3.0, 20.6 and 13.9 $M_\odot$, and within the redshifted lobes are 6.2, 11.9 and 8.9 $M_\odot$, respectively (see Table 8). Finally, the total mass of the outflows are: 24.9 $M_\odot$ for MM1, 78.8 $M_\odot$ for MM2, and 40.9 $M_\odot$ for MM3.

Using the standard LTE formalism, it is also possible to estimate the momentum, P, and the kinetic energy, $E_{\rm k}$, in the flow as follows (Margulis & Lada 1985; Bourke et al. 1997)

$$\begin{aligned} P &= \iiint M(v, \alpha, \delta)\, v\, dv\, d\alpha\, d\delta \ , \\ E_k &= \frac{1}{2} \iiint M(v, \alpha, \delta)\, v^2\, dv\, d\alpha\, d\delta \ . \end{aligned} \tag{10}$$

These equations assume no correction for flow inclination, and so are strict lower limits. Another method to compute the physical parameters of the outflowing gas is to assume that all the mass is flowing at a velocity characteristic of the entire flow, $V_{\rm char}$. The flow parameters are, in this approach, given by

$$P = M\ V_{\rm char}\ , \qquad E_{\rm k} = \frac{1}{2}\ M\ V_{\rm char}^2\ , \tag{11}$$

where M is the total mass of the outflow lobe. The blueshifted and redshifted emissions from the outflows show considerable overlap in their spatial distribution, indicating that the symmetry axis of the flows is likely to be near the line of sight. Hence, we adopt as a characteristic flow velocity the average of the maximum observed outflow velocities. The parameters determined under this assumption are likely to correspond to upper limits. The maximum velocities observed toward the blue and red lobes are, respectively, 12.0 and 23.1 km s^{-1} for the MM1 outflow, 15.0 and 15.9 km s^{-1} for the MM2 outflow, and 17.3 and 11.6 km s^{-1} for the MM3 outflow. Table 8 gives the derived parameters of the blueshifted gas and redshifted gas of the flows calculated using both methods. The geometric mean values for the outflow parameters are $\bar{P}_1 \sim 230$, $\bar{P}_2 \sim 690$, and $\bar{P}_3 \sim 270$ M$_\odot$ km s^{-1}; and $\bar{E}_{\rm k_1} \sim 1290$, $\bar{E}_{\rm k_2} \sim 3630$, and $\bar{E}_{\rm k_3} \sim 1120$ M$_\odot$ km^2 s^{-2} (subscripts 1, 2, and 3 refer to the MM cores). If the excitation temperature is increased to 50 K, the flow parameters increase by 7%. The derived values of the outflow parameters are similar to those of massive and energetic molecular outflows driven by high–mass young stellar objects (Shepherd & Churchwell 1996; Beuther et al. 2002; Wu et al. 2004). We do not provide estimates of the dynamical timescale, mechanical luminosity, and mass outflow rate of the outflows toward G34.43+0.24 because they are likely to be aligned close to the line of sight, and therefore the lengths of the lobes are difficult to estimate.

Rathborne et al. (2005) reported an excess 4.5 μm emission toward the MM cores. The *Spitzer* IRAC 4.5 μm band contains the H I Brα line (at 4.052 μm), the CO($1 \rightarrow 0$) P(8) band head (4.6–4.8μm), and many H_2 vibrational transitions (the most important being $H_2(0 \rightarrow 0)$ S(9) line at 4.694 μm), but unlike the other three bands it does not contain any strong polycyclic aromatic hydrocarbon (PAH) features (e.g., Smith et al. 2006). It has been postulated that the main contributers of the excess 4.5 μm emission could be emission from the CO($1 \rightarrow 0$) P(8) band head (e.g., Marston et al. 2004) and/or emission from the $H_2(0 \rightarrow 0)$ S(9) line (e.g., Noriega–Crespo et al. 2004). Thus, the enhancement of the 4.5 μm emission could be a probe of jets and molecular outflows (e.g., Teixeira et al. 2008; Smith et al. 2006; Noriega–Crespo et al. 2004); therefore of current star formation. Rathborne et al. (2005) first found evidence for the presence of high velocity gas toward the MM1 and MM3 cores from the broad line widths (ΔV ~10 km s^{-1}) observed in the CS($3 \rightarrow 2$) and HCN($3 \rightarrow 2$) lines. A detailed study of the central region of G34.43+0.24 was carried out by

Shepherd et al. (2007), who reported two molecular outflows emanating from MM1 (G34.4 MM, in their paper), and three outflows originating from the MM2 core. They estimate a total mass, momentum and kinetic energy of 34.8 $M_\odot$, 350 $M_\odot$ km s^{-1}, and 4.9×10^{46} ergs (2460 $M_\odot$ km^2 s^{-2}), for the outflows in MM1; and 111.2 $M_\odot$, 830 $M_\odot$ km s^{-1}, and 7.8×10^{46} ergs (3920 $M_\odot$ km^2 s^{-2}), for the outflows in MM2. The masses are ∼20% greater than our estimate, and the momenta and kinetic energies are within our estimated range. In spite of the different molecular transitions, angular resolutions and assumptions used, Shepherd et al. and our results are in agreement, within the observational errors.

4.2.1. The Discovery of a New Molecular Outflow Toward the Core G34.43+0.24 MM3

We report the discovery of one massive molecular outflow associated with the MM3 core discovered by Garay et al. (2004). They suggested that this massive and dense core, without counterpart at mid–infrared (*MSX*) and far–infrared (*IRAS*) wavelengths implying that it has a low temperature, seemed to be in a quiescent state, and thus appeared to be the youngest of the massive cores in the filament. The presence of 24 μm emission, a green fuzzy, water and methanol masers (Rathborne et al. 2005; Chambers et al. 2009) and the strong wing emission in the CO($3 \rightarrow 2$) line, indicating the presence of a powerful molecular outflow, all indicate star formation activity in the northernmost region of the filament. Due to its spatial location and mass, YSO number 29 in Shepherd et al. (2007) appears to be a good candidate for being the driver of the MM3–outflow. It is the most massive stellar object within MM3, with a mass of ∼4.8–6.8 $M_\odot$ and a luminosity of ∼170–340 $L_\odot$. However, this is an intermediate mass star that may not be able to drive alone the massive outflow. In the same region there are three more stars of intermediate mass (less massive than the number 29) with maximum masses between 4–5 $M_\odot$. Interferometric observations are needed to clarify if the MM3–outflow corresponds to an overlap of a few individual outflows, such as that seen in the central region of G34.43+0.24, or it is driven by a single star.

5. Conclusions

We carried out a multi–line study of cores within the filamentary IRDC G34.43+0.24. The emission from the filament was fully mapped in the CO($3 \rightarrow 2$) and ^{13}CO($3 \rightarrow 2$) lines. In addition, emission from the central region of the filament was observed in eight different molecular transitions [$C^{18}O(3 \rightarrow 2)$, $CS(7 \rightarrow 6)$, $CS(2 \rightarrow 1)$, $C^{34}S(2 \rightarrow 1)$, $HCO^+(1 \rightarrow 0)$, $H^{13}CO^+(1 \rightarrow 0)$, $SiO(2 \rightarrow 1)$ and $CH_3OH(2 \rightarrow 1)$], and from the north region in the $CS(2 \rightarrow 1)$ and $C^{18}O(3 \rightarrow 2)$ lines. The results of this study are summarized as follows.

The spatial distribution of the molecular emission in all, except methanol, lines is similar to that of the dust continuum emission derived from observations with similar angular resolution, showing a filamentary structure and four cores.

The mass of the molecular cores derived assuming LTE conditions are 300 and 1460 $M_\odot$ for the MM1 and MM2 cores, respectively. The masses derived assuming virial equilibrium are 1100, 1500 and 1400 $M_\odot$ for the MM1, MM2 and MM3 cores, respectively. The average molecular hydrogen densities of the cores are 1.8×10^5 cm^{-3} in MM1, 1.7×10^5 cm^{-3} in MM2 and 1.9×10^4 cm^{-3} in MM3. We also find that the molecular hydrogen column densities at the peak positions of MM1 and MM2 are, respectively, 2×10^{22} cm^{-2} and 8×10^{22} cm^{-2}. The derived parameters of the MM1 and MM2 cores are typical of massive and dense cores harboring high-mass YSO's (Plume et al. 1997; Garay et al. 2007). Those of the MM3 core suggest that it harbors young intermediate mass stars, in accord with the result obtained by Shepherd et al. (2007) from the modeling of the SED of the NIR sources detected using *Spitzer*.

We modeled the molecular emission in the ^{13}CO$(3\rightarrow2)$, C^{18}O$(3\rightarrow2)$, and CS$(7\rightarrow6)$ lines toward the MM2 core, concluding that this core is undergoing infalling motions, with an infall velocity of $\sim$1.3 km s^{-1} and a mass infall rate of $\sim1.8\times10^{-3}$ $M_\odot$ yr^{-1}. This value is large enough to allow the formation of massive stars by accretion (see Osorio, Lizano & D'Alessio 1999).

We report the discovery of a molecular outflow associated with the massive, dense MM3 core located in the northern region of G34.43+0.24, and possibly of a second one associated with the MM4 core. The molecular outflow within MM3 has a total mass of 41 $M_\odot$, a momentum of 270 $M_\odot$ km s^{-1}, and a kinetic energy of 1120 $M_\odot$ km^2 s^{-2}; indicating that it is driven by high–intermadiate mass stars. We also detected high velocity molecular gas toward the MM1 and MM2 cores with total masses of 25 and 80 $M_\odot$, momenta of 230 and 690 $M_\odot$ km s^{-1}, and kinetic energies of 1290 and 3630 $M_\odot$ km^2 s^{-2}, respectively.

The authors gratefully acknowledge support from CONICYT projects FONDAP No. 15010003 and BASAL PFB-06.

REFERENCES

Beuther, H., Schilke, P., Sridharan, T. K., Menten, K. M., Walmsley, C. M., & Wyrowski, F. 2002, A&A, 383, 892

Bourke, T. L., Garay, G., Lehtinen, K. K., Köhnenkamp, I., Launhardt, R., Nyman, L.-Å., May, J., Robinson, G., & Hyland, A. R. 1997, ApJ, 476, 781

Bronfman, L., Nyman, L.-Å., & May, J. 1996, A&AS, 115, 81

Carey, S. J., Clark, F. O., Egan, M. P., Price, S. D., Shipman, R. F., & Kuchar, T. A. 1998, ApJ, 508, 721

Carey, S. J., Feldman, P. A., Redman, R. O., Egan, M. P., MacLeod, J. M., & Price, S. D. 2000, ApJ, 543, L157

Chambers, E. T., Jackson, J. M., Rathborne, J. M., & Simon, R. 2009, ApJS, 181, 360

Cortes, P., Crutcher, R. M., Shepherd, D. S., & Bronfman, L. 2008, ApJ, 676, 464

Egan, M. P., Shipman, R. F., Price, S. D., Carey, S. J., Clark, F. O., & Cohen, M. 1998, ApJ, 494, L199

Evans, II, N. J. 1999, ARA&A, 37, 311

Faúndez, S., Bronfman, L., Garay, G., Chini, R., Nyman, L.-Å., & May, J. 2004, A&A, 426, 97

Frerking, M. A., Langer, W. D., & Wilson, R. W. 1982, ApJ, 262, 590

Fuller, G. A., Williams, S. J., & Sridharan, T. K. 2005, A&A, 442, 949

Garay, G., & Lizano, S. 1999, PASP, 111, 1049

Garay, G., Faúndez, S., Mardones, D., Bronfman, L., Chini, R., & Nyman, L.-Å. 2004, ApJ, 610, 313

Garay, G., Mardones, D., Brooks, K. J., Videla, L., & Contreras, Y. 2007, ApJ, 666, 309

Garden, R. P., Hayashi, M., Hasegawa, T., Gatley, I., & Kaifu, N. 1991, ApJ, 374, 540

Hartquist, T. W., Dalgarno, A., & Oppenheimer, M. 1980, ApJ, 236, 182

Hennebelle, P., Pérault, M., Teyssier, D., & Ganesh, S. 2001, A&A, 365, 598

Jackson, J. M., Finn, S. C., Rathborne, J. M., Chambers, E. T., & Simon, R. 2008, ApJ, 680, 349

MacLaren, I., Richardson, K. M., & Wolfendale, A. W. 1988, ApJ, 333, 821

Mardones, D., Myers, P. C., Tafalla, M., Wilner, D. J., Bachiller, R., & Garay, G. 1997, ApJ, 489, 719

Margulis, M. & Lada, C. J. 1985, ApJ, 299, 925

Marston, A. P., et al. 2004, ApJS, 154, 333

Miralles, M. P., Rodríguez, L. F., & Scalise, E. 1994, ApJS, 92, 173

Molinari, S., Brand, J., Cesaroni, R., & Palla, F. 1996, A&A, 308, 573

Molinari, S., Brand, J., Cesaroni, R., Palla, F., & Palumbo, G. G. C. 1998, A&A, 336, 339

Myers, P. C., Mardones, D., Tafalla, M., Williams, J. P., & Wilner, D. J. 1996, ApJ, 465, L133

Noriega-Crespo, A., Morris, P., Marleau, F. R., Carey, S., Boogert, A., van Dishoeck, E., Evans, II, N. J., Keene, J., Muzerolle, J., Stapelfeldt, K., Pontoppidan, K., Lowrance, P., Allen, L., & Bourke, T. L. 2004, ApJS, 154, 352

Osorio, M., Lizano, S., & D'Alessio, P. 1999, ApJ, 525, 808

Perault, M., et al. 1996, A&A, 315, L165

Pillai, T., Wyrowski, F., Carey, S. J., & Menten, K. M. 2006, A&A, 450, 569

Plume, R., Jaffe, D. T., Evans, N. J. II, Martín–Pintado, J., & Gómez–Gonzáles, J. 1997, ApJ, 476, 730

Ramesh, B., Bronfman, L., & Deguchi, S. 1997, PASJ, 49, 307

Rathborne, J. M., Jackson, J. M., Chambers, E. T., Simon, R., Shipman, R., & Frieswijk, W. 2005, ApJ, 630, L181

Rathborne, J. M., Jackson, J. M., Simon, R. 2006, ApJ, 641, 389

Rathborne, J. M., Simon, R., & Jackson, J. M. 2007, ApJ, 662, 1082

Rathborne, J. M., Jackson, J. M., Zhang, Q., & Simon, R. 2008, ApJ, 689, 1141

Shepherd, D. S., & Churchwell, E. 1996, ApJ, 472, 225

Shepherd, D. S., Nürnberger, D. E. A., Bronfman, L. 2004, ApJ, 602, 850

Shepherd, D. S., Povich, M. S., Whitney, B. A., Robitaille, T. P., Nürnberger, D. E. A., Bronfman, L., Stark, D. P., Indebetouw, R, Meade, M. R., & Babler, B. L. 2007, ApJ, 669, 464

Simon, R., Jackson, J. M., Rathborne, J. M., & Chambers, E. T. 2006a, ApJ, 639, 227

Simon, R., Rathborne, J. M., Shah, R. Y., Jackson, J. M., & Chambers, E. T. 2006b, ApJ, 653, 1325

Smith, H. A., Hora, J. L., Marengo, M., & Pipher, J. L. 2006, ApJ, 645, 1264

Szymczak, M., Hrynek, G., & Kus, A. J. 2000, A&AS, 143, 269

Teixeira, P. S., McCoey, C., Fich, M., & Lada, C. J. 2008, MNRAS, 384, 71

Turner, J. L. & Dalgarno, A. 1977, ApJ, 213, 386

van der Tak, F. F. S., van Dishoeck, E. F., Evans, II, N, J., & Blake, G. A. 2000, ApJ, 537, 283

Wang, Y., Zhang, Q., Rathborne, J. M., Jackson, J., & Wu, Y. 2006, ApJ, 651, L125

Wilson, T. L., & Rood, R. 1994, ARA&A, 32, 191

Wu, Y., Wei, Y., Zhao, M., Shi, Y., Yu, W., Qin, S., & Huang, M. 2004, A&A, 426, 503

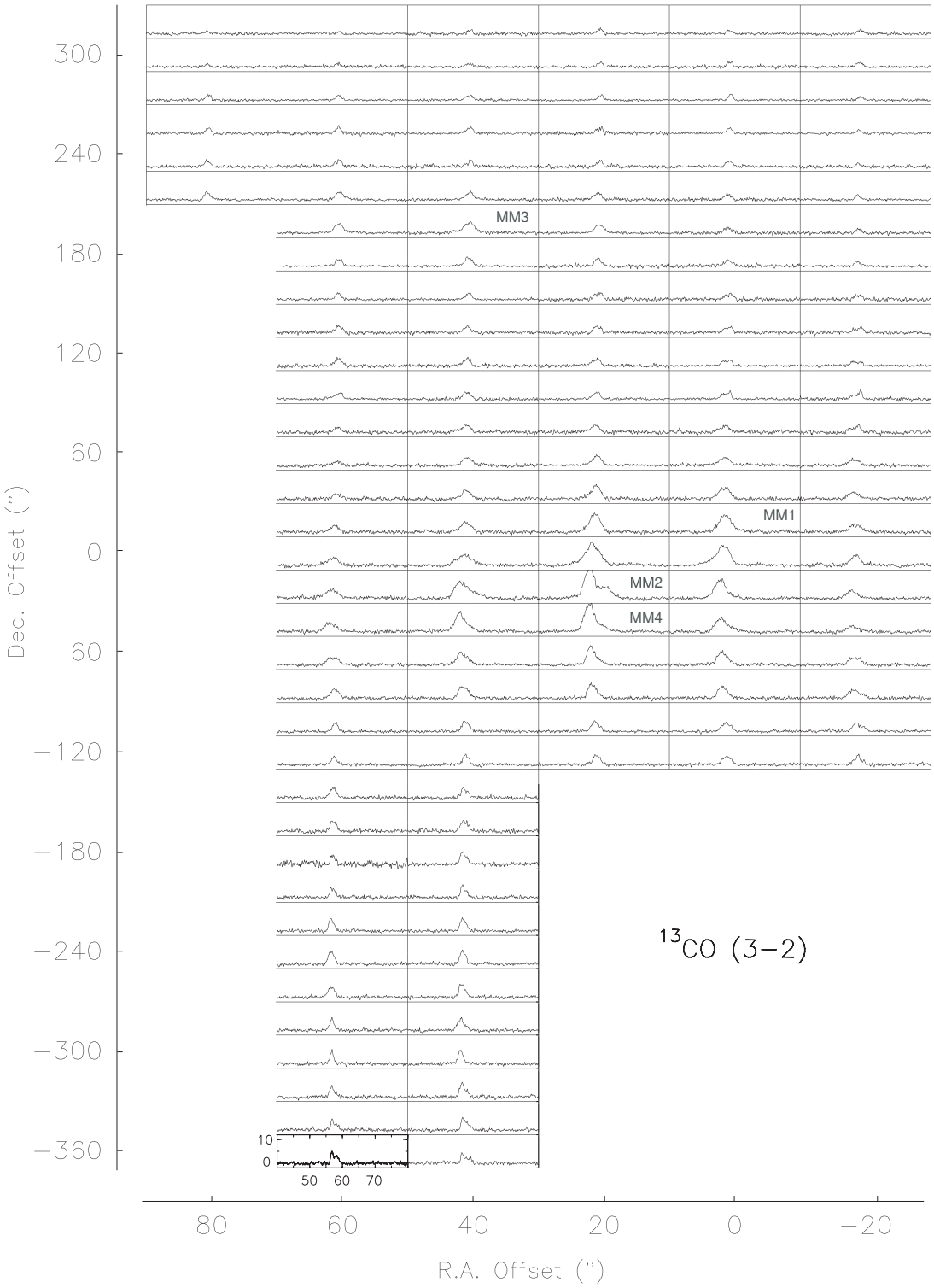

Fig. 1.— Observed spectra of the ^{13}CO($3 \rightarrow 2$) line emission toward G34.43+0.24, taken with the APEX telescope. The angular separation between panels is 20″. Offsets are from the reference position at $\alpha = 18^h53^m17.^s40$ and $\delta = 01°24'55''$ (J2000). In each box the velocity scale ranges from 40 to 80 km s^{-1}. The antenna temperature scale is from -2 to 12 K.

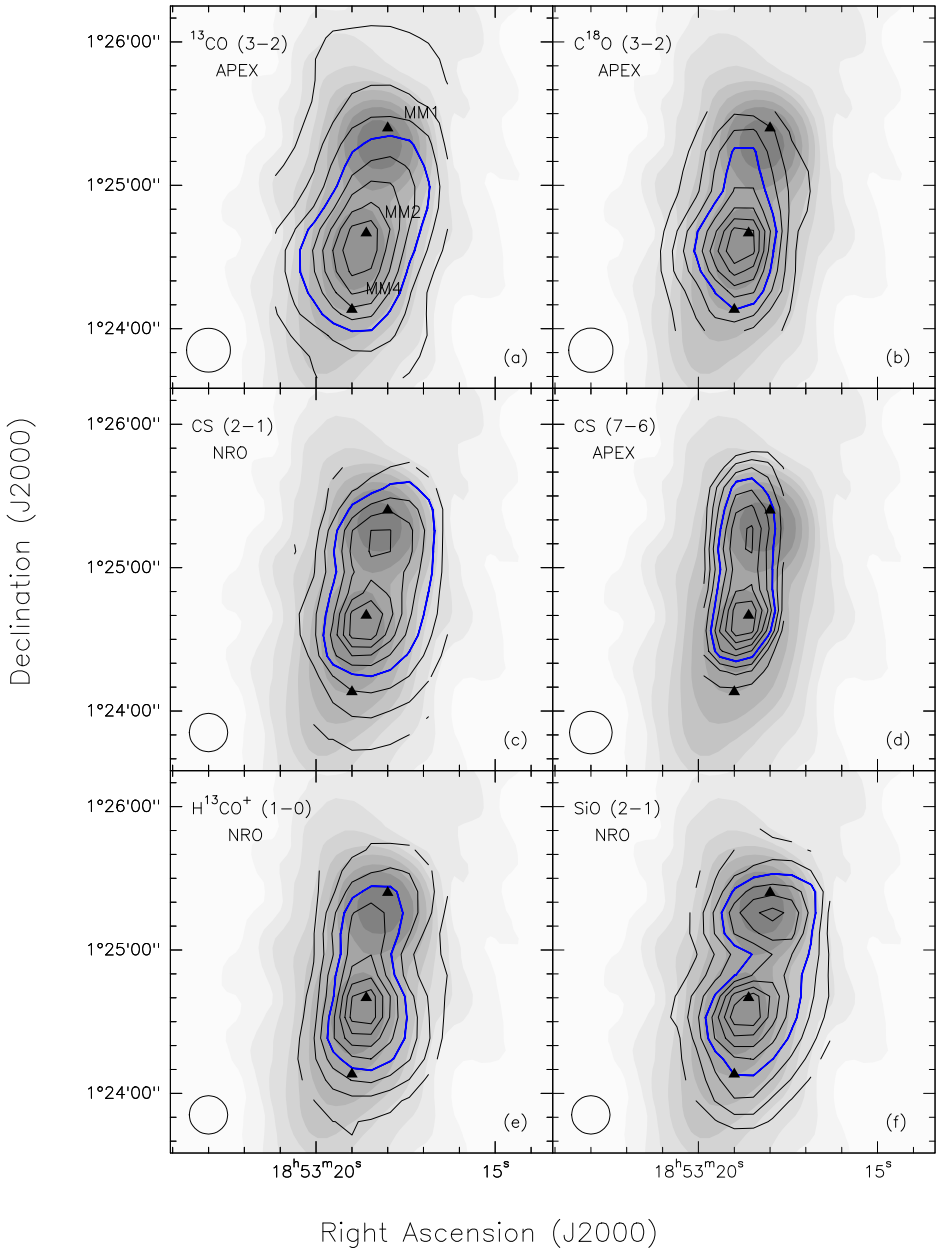

Fig. 2.— Contour maps of velocity-integrated ambient molecular emission toward the central region of G34.43+0.24, overlaid on a 1.2 mm dust continuum emission map (gray scale). The range of integration in v_{lsr} is from 52.9 to 61.1 km s^{-1}. The FWHM beam is shown in the bottom left corner. Contour levels are from 20% to 90% (in steps of 10%) of the peak integrated intensity of 49.9 K km s^{-1} for ^{13}CO($3 \rightarrow 2$) (*a*); 7.7 K km s^{-1} for CS($7 \rightarrow 6$) (*b*); 16.9 K km s^{-1} for CS($2 \rightarrow 1$) (*c*); 3.4 K km s^{-1} for SiO($2 \rightarrow 1$) (*d*); 3.7 K km s^{-1} for H^{13}CO$^+$($1 \rightarrow 0$) (*e*); and 14.3 K km s^{-1} for C^{18}O($3 \rightarrow 2$) (*f*). The blue lines indicate the 50% contour level. The gray scale levels are 1, 2, 3, 5, 7, 10, 15, 20 and 30 $\times$ 0.12 Jy beam^{-1}. The triangles mark the peak positions of the MM1, MM2 and MM4 dust cores.

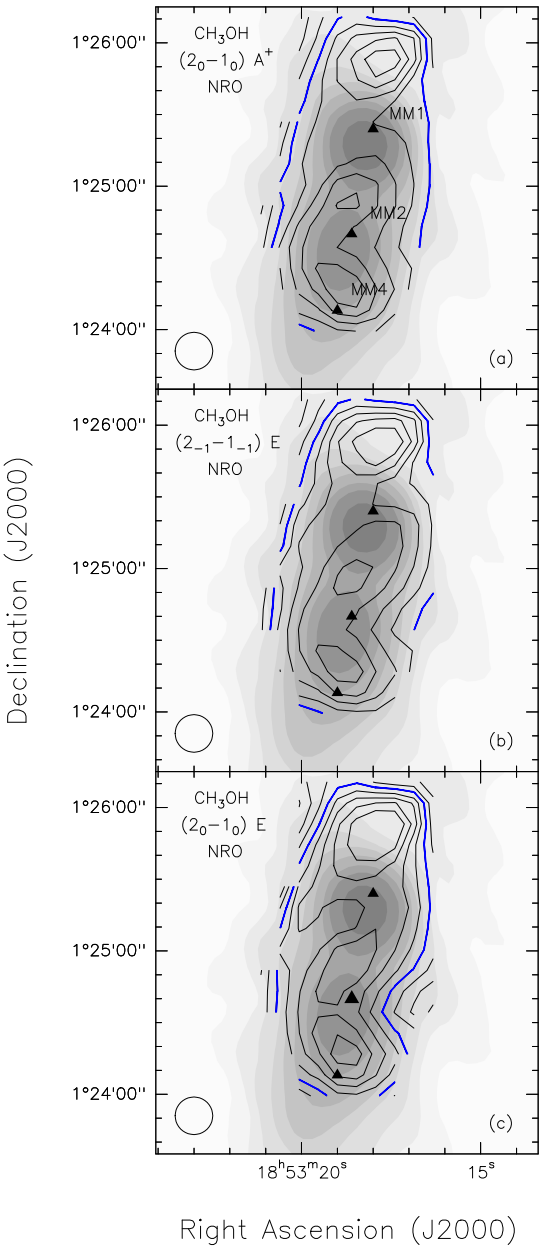

Fig. 3.— Contour maps of velocity-integrated ambient CH_3OH emission toward the central region of G34.43+0.24, overlaid on a 1.2 mm dust continuum emission map (gray scale). The FWHM beam is shown in the bottom left corner. Contour levels are from 20% to 90% (in steps of 10%) of the peak integrated intensity of 5.1 K km s^{-1} for $CH_3OH(2_0 \rightarrow 1_0)$ A+ (*a*); 4.1 K km s^{-1} for $CH_3OH(2_{-1} \rightarrow 1_{-1})$ E (*b*); and 1.1 K km s^{-1} for $CH_3OH(2_0 \rightarrow 1_0)$ E (*c*). The blue lines indicate the 50% contour level. The gray scale levels are 1, 2, 3, 5, 7, 10, 15, 20 and 30 × 0.12 Jy beam^{-1}. The triangles mark the peak positions of the MM1, MM2 and MM4 dust cores.

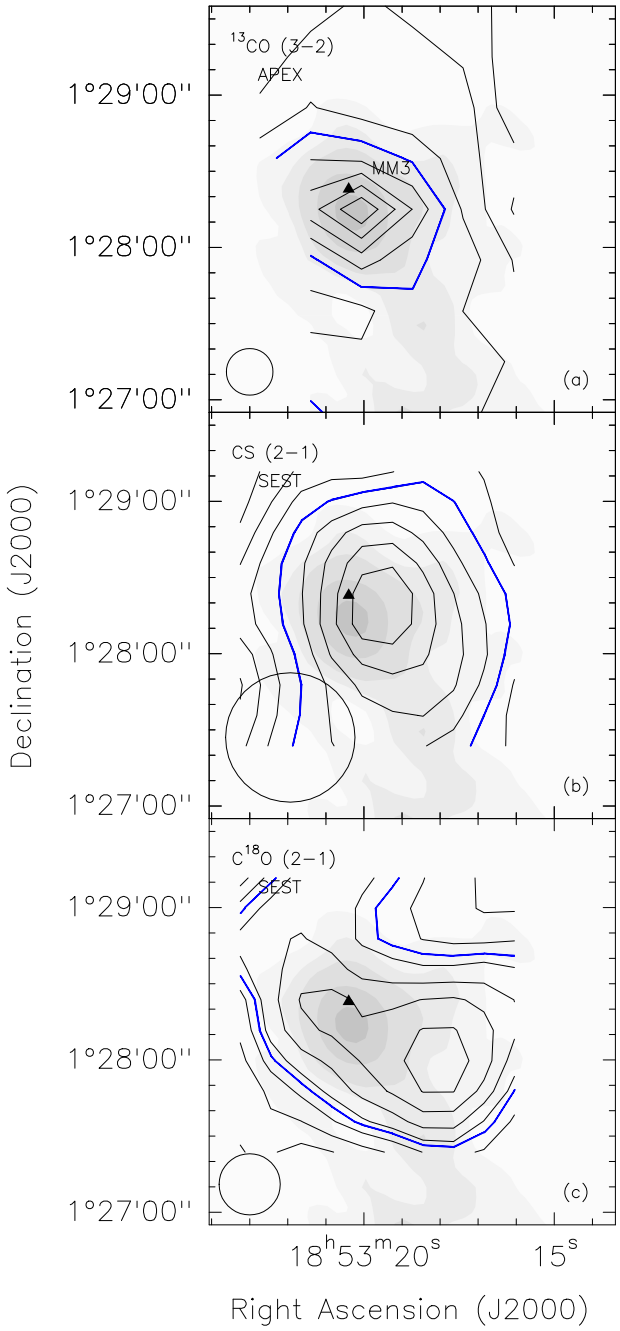

Fig. 4.— Contour maps of velocity-integrated molecular line emission toward the MM3 core (Garay et al. 2004), overlaid on a 1.2 mm dust continuum emission map (gray scale). The range of integration in v_{lsr} is from 56.1 to 61.5 km s^{-1}. Contour levels are from 20% to 90% (in steps of 10%) of the peak integrated intensity of 12.5 K km s^{-1} for ^{13}CO($3 \rightarrow 2$) (*a*) and 3.7 K km s^{-1} for CS($2 \rightarrow 1$) (*b*); and from 3 to 21 σ in steps 3 σ, with $\sigma = 0.14$ K km s^{-1}, for C^{18}O($2 \rightarrow 1$) (*c*). The gray scale levels are 1, 2, 3, 5, 7, 10, 15, 20 and 30 $\times$ 0.12 Jy beam^{-1}. The blue lines indicate the 50% contour level. The triangle marks the peak position of the MM3 core. The FWHM beam is shown in the bottom left corner.

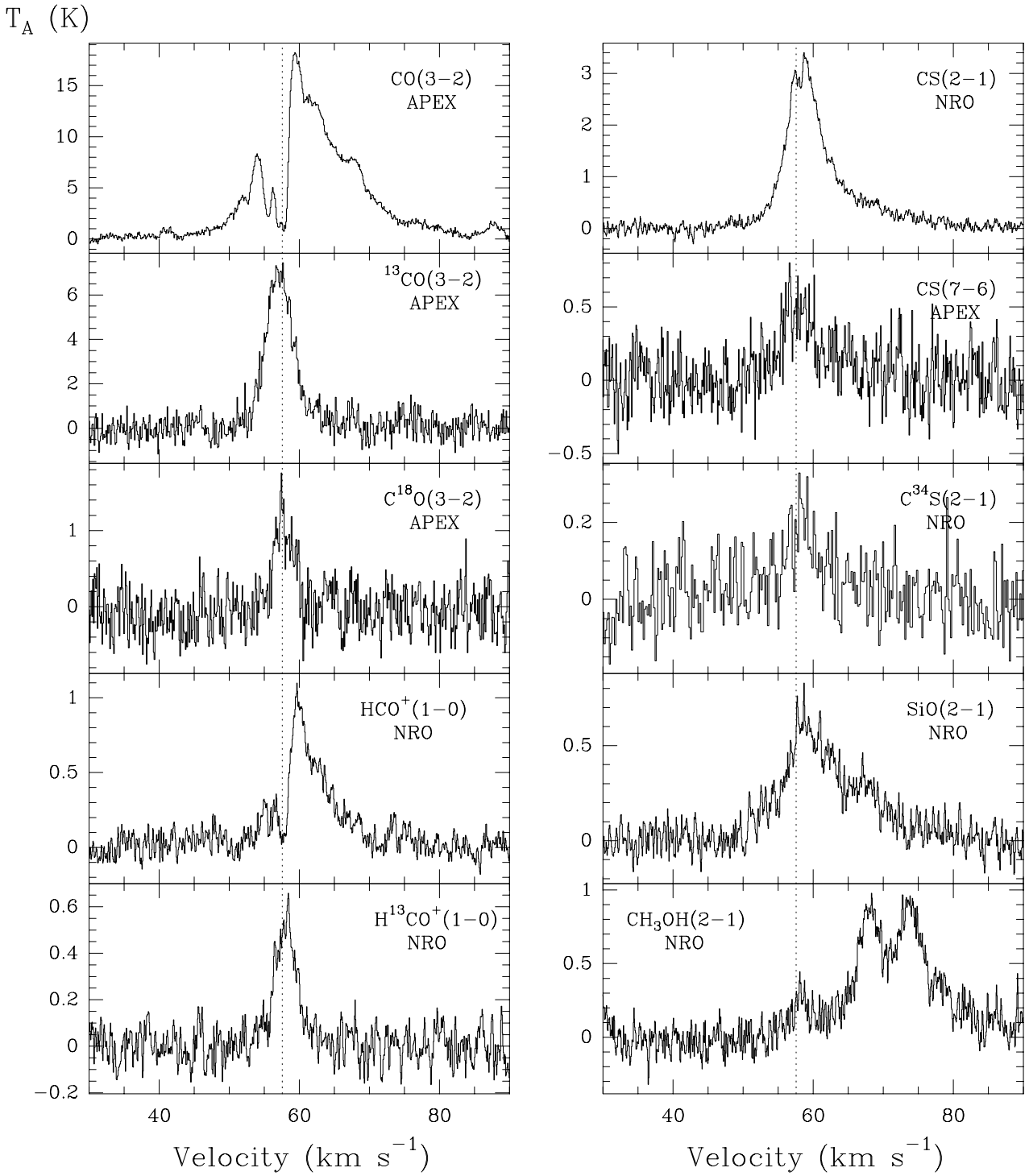

Fig. 5.— Molecular spectra observed toward the peak position of the millimeter continuum of MM1 core. Transitions and telescopes are given in the top corner of the spectra. The vertical dotted line indicates the systemic velocity of the ambient gas of 57.6 km s^{-1} (Miralles, Rodríguez & Scalise 1994).

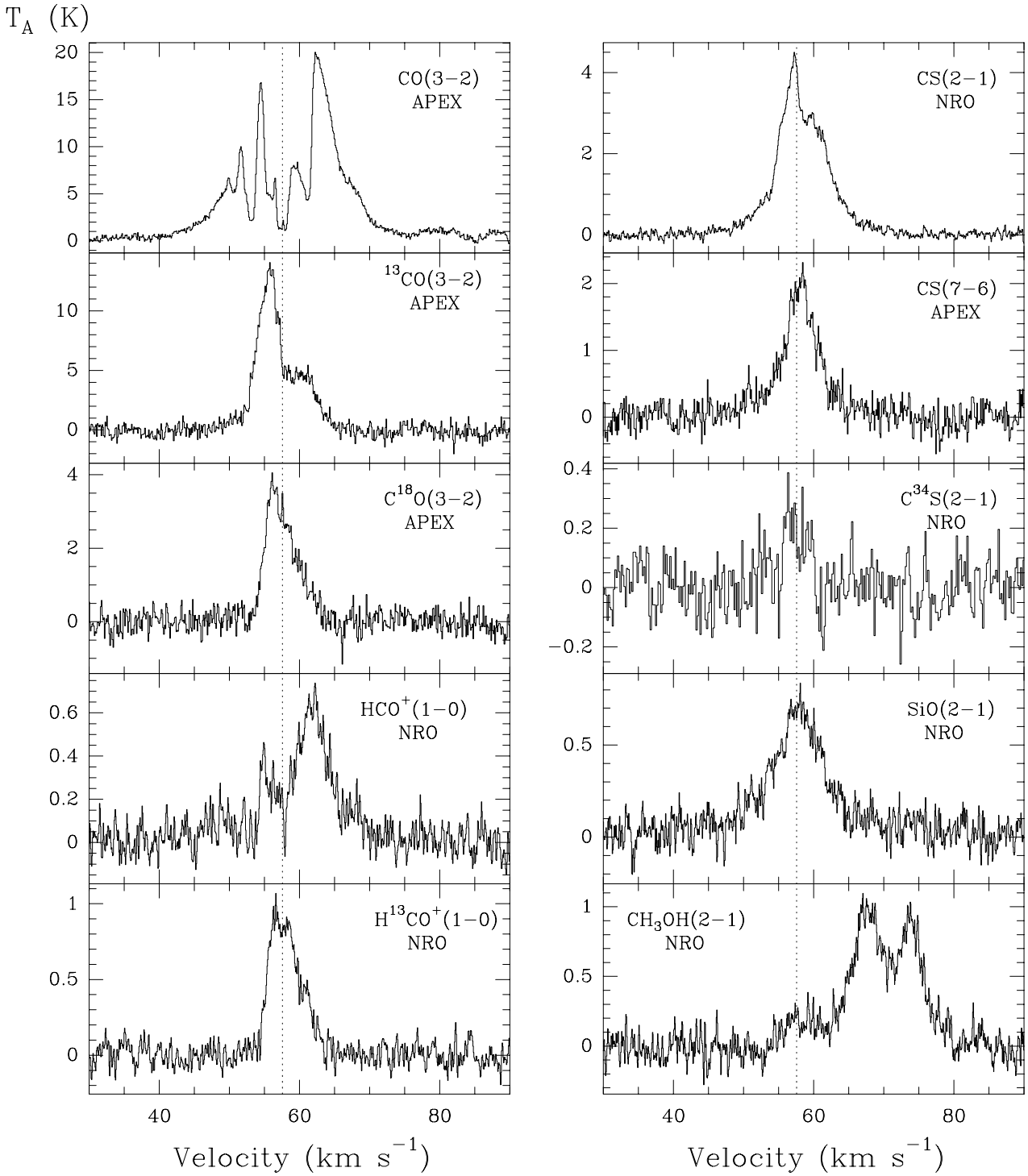

Fig. 6.— Molecular spectra observed toward the peak position of the millimeter continuum of MM2 core (IRAS 18507+0121). Transitions and telescopes are given in the top corner of the spectra. The vertical dotted line indicates the systemic velocity of the ambient gas of 57.6 km s^{-1} (Miralles, Rodríguez & Scalise 1994).

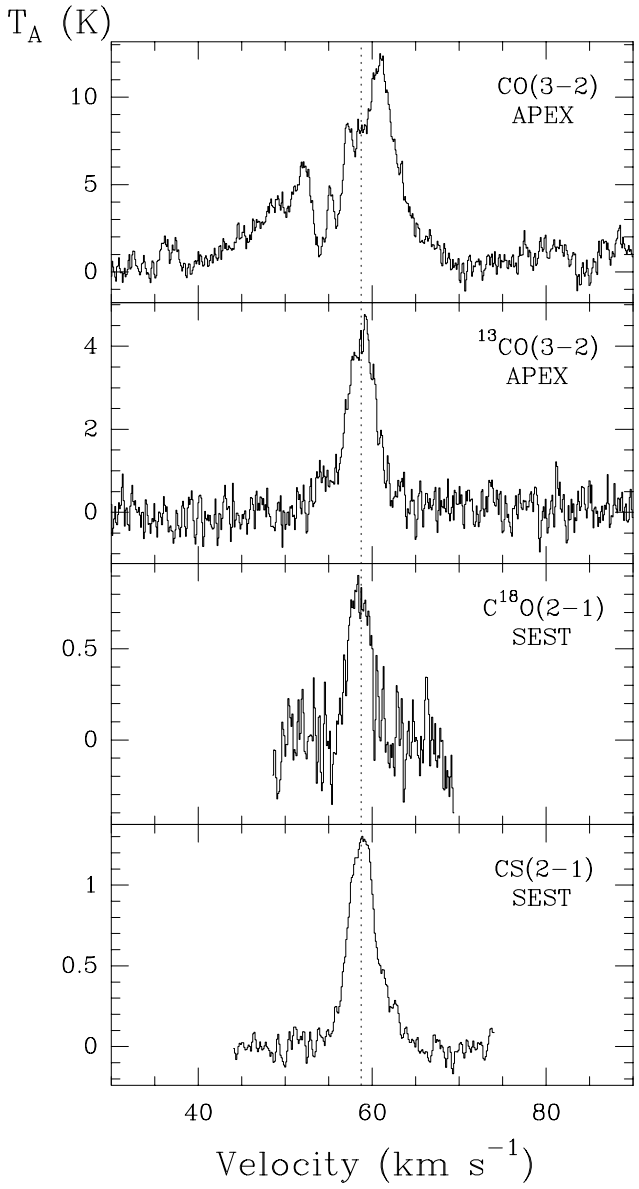

Fig. 7.— Molecular spectra observed toward the peak position of the millimeter continuum of MM3 core. Transitions and telescopes are given in the top right corner of the spectra. The vertical dotted line indicates the systemic velocity of the ambient gas of 58.7 km s^{-1} (estimated from the optically thin $^{13}CO(3 \rightarrow 2)$, $C^{18}O(2 \rightarrow 1)$ and $CS(2 \rightarrow 1)$ lines).

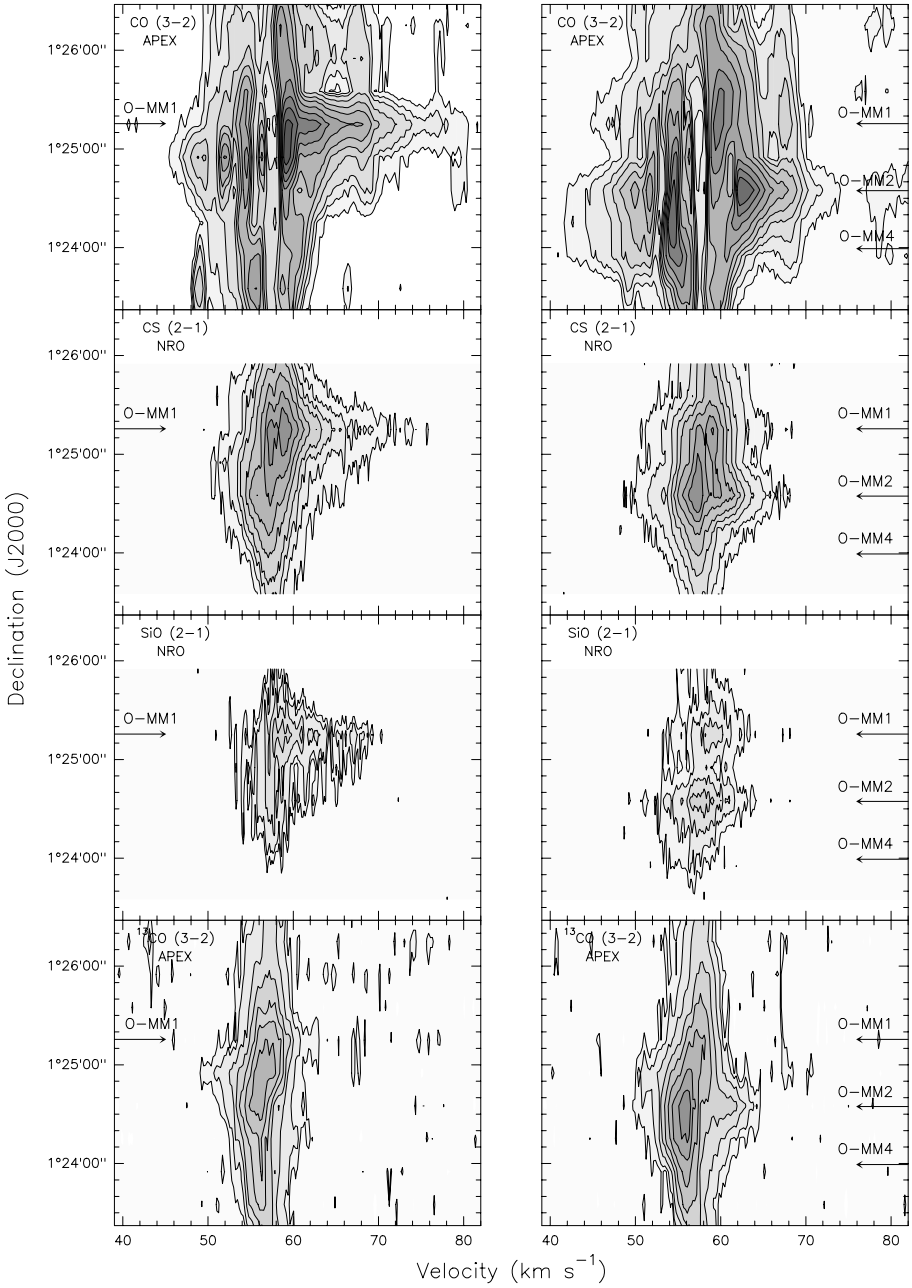

Fig. 8.— Position-velocity diagrams along lines in the north-south direction (i.e., parallel to the filament). Transitions and telescopes are indicated in the top left corner of each panel. *Left*: Cut passing through MM1 or position (0″, 20″). Contour levels are 3, 9, 15, 23, 31, 41, 51, and 61 × 0.27 K for CO(3 → 2); 3, 6, 9, 12, 17, 22, 28, and 34 × 0.08 K for CS(2 → 1); 3, 4, 6, and 8 × 0.07 K for SiO(2 → 1); and 1.5, 3, 6, 9, 12, 15, and 19 × 0.37 K for ^{13}CO(3 → 2). *Right*: Cut passing through MM2 or position (20″, 0″). Contour levels are 3, 8, 13, 18, 28, 38, 48, and 58 × 0.27 K for CO(3 → 2); 3, 6, 11, 16, 21, 28, 35, and 42 × 0.08 K for CS(2 → 1); 3, 5, 7, and 9 × 0.07 K for SiO(2 → 1); and 1.5, 3, 6, 10, 14, 19, 25, and 31 × 0.37 K for ^{13}CO(3 → 2).

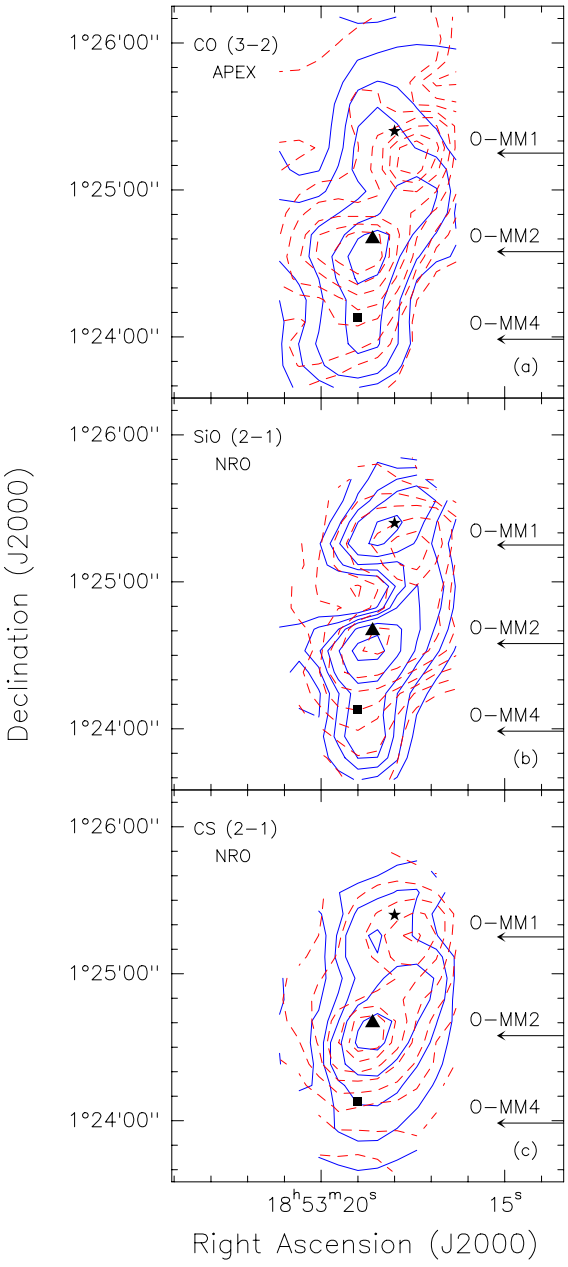

Fig. 9.— Contour maps of velocity-integrated wing emission toward the central region of G34.43+0.24, in different molecular lines. Transitions and telescopes are indicated in the top left corner of each panel. The arrows in the panels indicate where are the outflows corresponding to each core. Contour levels for the blueshifted emission are 20, 35, 50, 80, and 110 σ for CO($3 \rightarrow 2$); 3, 5, 7, 9, 12, and 16 σ for SiO($2 \rightarrow 1$); and 3, 9, 15, 25, and 40 σ for CS($2 \rightarrow 1$). For the redshifted emission, these are 20, 35, 50, 80, 110, 150, 190, and 230 σ for CO($3 \rightarrow 2$); 3, 5, 7, 9, 12, 16, 24, and 32 σ for SiO($2 \rightarrow 1$); and 3, 9, 15, 25, 40, 60, 85, and 110 σ for CS($2 \rightarrow 1$). The σ values are: 0.30 K km s^{-1} for the CO line, and 0.04 K km s^{-1} for the SiO and CS lines.

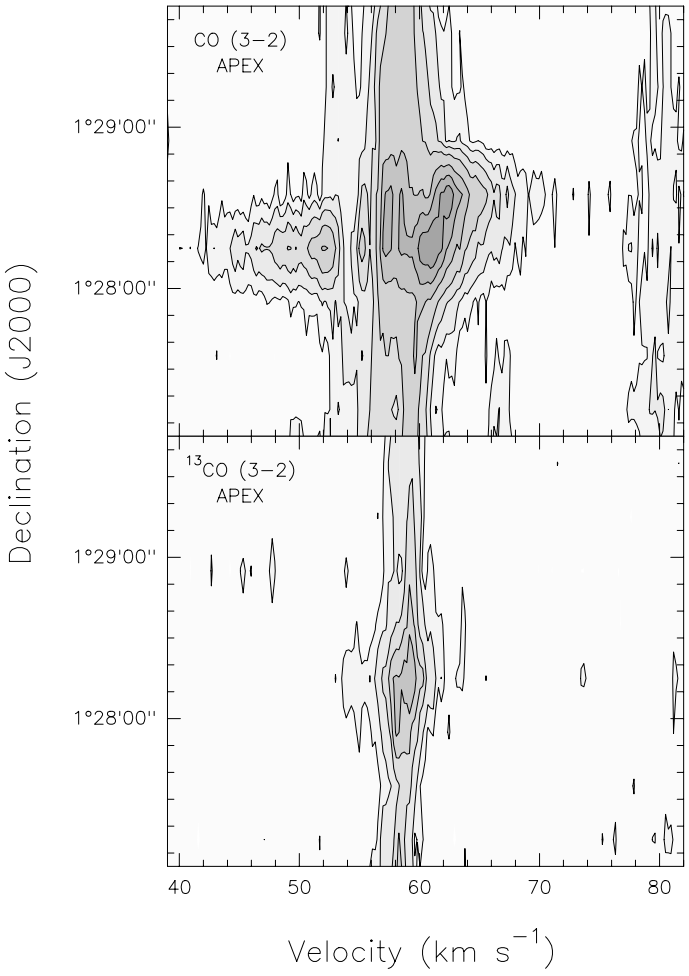

Fig. 10.— Position-velocity diagrams of CO($3 \rightarrow 2$) and ^{13}CO($3 \rightarrow 2$) toward the northernmost region of G34.43+0.24 along a line running since the north-south direction passing through of MM3 (position (40″, 0″) in Figure 1). Transitions and telescopes are indicated in the top left corner of each panel. The contour levels for CO($3 \rightarrow 2$) are 3, 6, 10, 15, 22, 29 and 36 σ, with $\sigma = 0.27$ K. For ^{13}CO($3 \rightarrow 2$) are 1.5, 3, 6, 8 and 10 σ, with $\sigma = 0.37$ K.

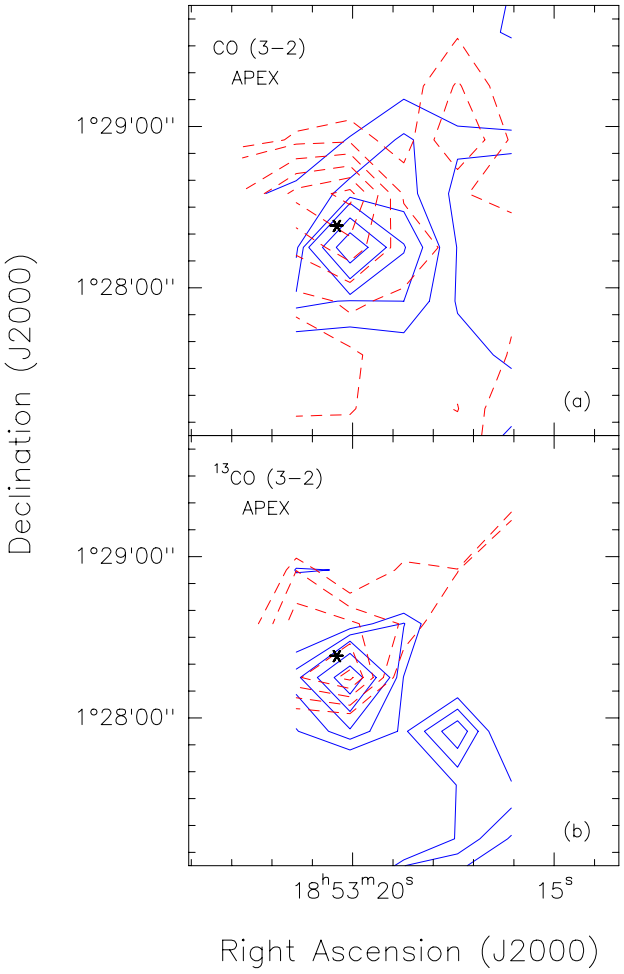

Fig. 11.— Contour maps of velocity-integrated wing emission of CO($3 \rightarrow 2$) and ^{13}CO($3 \rightarrow 2$) toward the northernmost region of G34.43+0.24. Solid lines represent blueshifted emission and dashed lines represent redshifted emission. The asterisk shows the position of the MM3 core. *Top*: CO($3 \rightarrow 2$) emission. Contour levels for the blueshifted emission are 20, 30, 40, 50, 75 and 100 σ ($\sigma = 0.35$ K km s^{-1}); and for redshifted emission, these are 20, 30, 60, 90, 120 and 150 σ ($\sigma = 0.25$ K km s^{-1}). *Bottom*: ^{13}CO($3 \rightarrow 2$) emission. Contour levels for the blueshifted emission are 3, 4, 5, 7 and 9 σ ($\sigma = 0.23$ K km s^{-1}); and for redshifted emission, these are 3, 4, 5, 6 and 7 σ ($\sigma = 0.19$ K km s^{-1}).

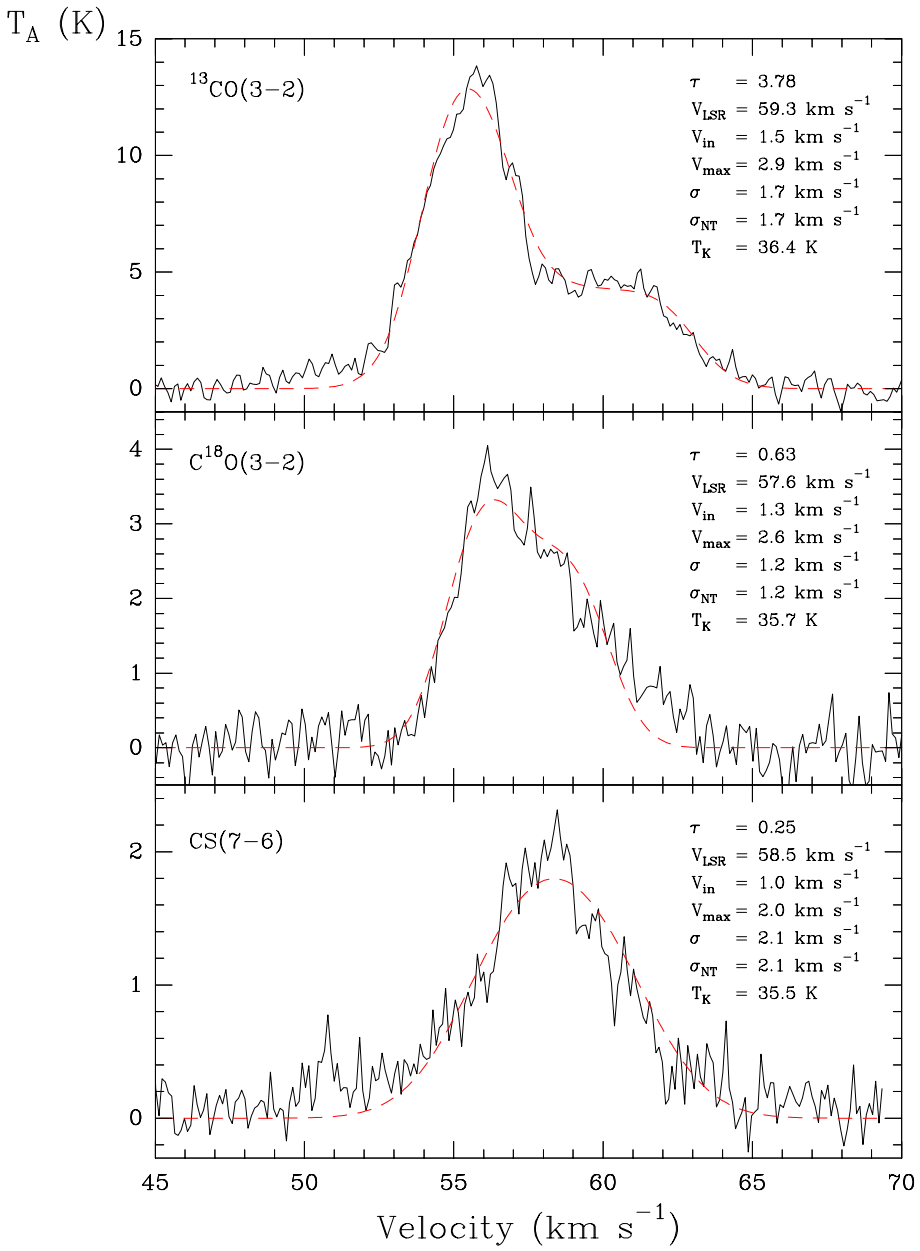

Fig. 12.— ^{13}CO($3 \rightarrow 2$), C^{18}O($3 \rightarrow 2$), and CS($7 \rightarrow 6$) spectra of the MM2 peak position with the simple two layer model fits of Myers et al. (1996). The solid lines show the observed spectra and the dashed (red) lines represent the model. The values derived by the model are shown in the right side of the figure.

Table 1: Properties of 1.2 mm Cores

	Peak Position		FWHM Diameter		
	α(J2000)	δ(J2000)	Angular	Physical	Mass
Core			($''$)	(pc)	$M_\odot$
MM1	18 53 18.0	01 25 24	16	0.19	1187
MM2	18 53 18.6	01 24 40	26	0.42	1284
MM3	18 53 20.4	01 28 23	24	0.38	301
MM4	18 53 19.0	01 24 08	24	0.38	253

Note. — Units of right ascension are hours, minutes and seconds, and units of declination are degrees, arcminutes and arcseconds.

Note. — Properties adopted from Rathborne, Jackson & Simon (2006).

Table 2: Summary of Observational Parameters

Observation	Frequency (GHz)	Beam (FWHM) (arcsec)	Spacing (arcsec)	Observed Positions	Region Size (arcsec^2)	Δv (km s^{-1})	rms Noise (T_A) (K)
			APEX				
$^{13}CO(3 \rightarrow 2)$...	330.588	18.4	20	145[a]	120×700	0.11	0.37
$CO(3 \rightarrow 2)$.....	345.796	17.6	20	145[a]	120×700	0.11	0.27
$CS(7 \rightarrow 6)$	342.883	17.8	20	21[b]	60×140	0.11	0.18
$C^{18}O(3 \rightarrow 2)$...	329.331	18.5	20	30[b]	100×120	0.11	0.29
			Nobeyama				
$CS(2 \rightarrow 1)$	97.981	15.5	20	30[b]	100×160	0.11	0.08
$SiO(2 \rightarrow 1)$.....	86.846	17.7	20	30[b]	100×160	0.13	0.07
$C^{34}S(2 \rightarrow 1)$ ...	96.412	15.8	20	31[b]	100×160	0.12	0.10
$HCO^+(1 \rightarrow 0)$..	89.188	17.3	20	31[b]	100×160	0.12	0.08
$H^{13}CO^+(1 \rightarrow 0)$	86.754	17.7	20	30[b]	100×160	0.13	0.07
$CH_3OH(2 \rightarrow 1)$	96.744	15.7	20	31[b]	100×160	0.12	0.09
			SEST				
$CS(2 \rightarrow 1)$	97.981	51.0	30	25[c]	100×100	0.13	0.07
$C^{18}O(2 \rightarrow 1)$...	219.560	24.1	30	25[c]	100×100	0.12	0.18

[a]Covering the whole filamentary structure.

[b]Covering the central region of G34.43+0.24, including the MM1, MM2 and MM4 cores.

[c]Covering the MM3 core, in the northern region of the G34.43+0.24 filament.

Table 3. Observed Parameters of Molecular Cores

Core	Molecular Transition	Angular Size ($'' \times ''$)	v_{lsr} (km s^{-1})	ΔV (km s^{-1})	$\int T_{mb} dv$ (K km s^{-1})	Physical Size (pc^2)
MM1	CS($7 \rightarrow 6$)	37.2×20.6	57.38 ± 0.21	5.69 ± 0.71	6.94 ± 0.80	0.66×0.38
	CS($2 \rightarrow 1$)	45.4×33.0	58.13 ± 0.01	5.29 ± 0.02	15.10 ± 0.04	0.82×0.60
	$H^{13}CO^+(1 \rightarrow 0)$	33.0×24.8	58.36 ± 0.02	2.75 ± 0.06	2.78 ± 0.05	0.60×0.44
MM2	CS($7 \rightarrow 6$)	37.2×24.8	57.96 ± 0.03	5.27 ± 0.09	9.41 ± 0.13	0.66×0.44
	CS($2 \rightarrow 1$)	41.2×37.2	57.35 ± 0.01	5.19 ± 0.03	15.41 ± 0.07	0.74×0.66
	$H^{13}CO^+(1 \rightarrow 0)$	41.2×33.0	57.88 ± 0.02	3.96 ± 0.05	3.52 ± 0.04	0.74×0.60
MM3	^{13}CO($3 \rightarrow 2$)...	74.2×53.6	58.77 ± 0.02	3.01 ± 0.04	10.31 ± 0.11	1.34×0.96
	CS($2 \rightarrow 1$)	86.6×70.0	58.73 ± 0.01	3.43 ± 0.03	3.44 ± 0.02	1.54×1.24

Table 4: Derived LTE Core Parameters

Core	Transition	τ_ν	N[a] (cm^{-2})	$N(H_2)$ (cm^{-2})	M_{LTE} ($M_\odot$)
MM1	$C^{18}O(3 \rightarrow 2)$	0.10	5.2×10^{15}	2.0×10^{22}	330
	$^{13}CO(3 \rightarrow 2)$	0.75	3.9×10^{16}		
MM2	$C^{18}O(3 \rightarrow 2)$	0.18	1.1×10^{16}	4.3×10^{22}	1460
	$^{13}CO(3 \rightarrow 2)$	1.39	8.7×10^{16}		

Note. — Velocity range for the MM1 core: 54.6–59.3 km s^{-1}.
Velocity range for the MM2 core: 53.4–59.3 km s^{-1}.

[a]Column density for each molecule.

Table 5: Derived Virial Core Parameters

Core	Transition	Radius[a] (pc)	ΔV (km s^{-1})	M_{vir} ($M_\odot$)	n(H_2) (cm^{-3})
MM1	$CS(7 \rightarrow 6)$.....	0.25	5.69	1700	3.9×10^5
	$CS(2 \rightarrow 1)$.....	0.35	5.29	2060	1.7×10^5
	$H^{13}CO^+(1 \rightarrow 0)$	0.26	2.75	410	8.3×10^4
MM2	$CS(7 \rightarrow 6)$.....	0.27	5.27	1580	2.8×10^5
	$CS(2 \rightarrow 1)$.....	0.35	5.19	1980	1.6×10^5
	$H^{13}CO^+(1 \rightarrow 0)$	0.33	3.96	1090	1.1×10^5
MM3	$^{13}CO(3 \rightarrow 2)$...	0.57	3.01	1090	2.1×10^4
	$CS(2 \rightarrow 1)$.....	0.69	3.43	1710	1.8×10^4

[a]Geometric mean of the observed semi-major and semi-minor axes.

Table 6: Core Masses from Different Authors

	LTE Mass	Virial Mass	LTE Mass	Dust Mass (1.2 mm)	
Core	(This work)	(This work)	Shepherd et al. (2007)	Garay et al. (2004)	Rathborne et al. (2006)
(1)	(2)	(3)	(4)	(5)	(6)
MM1	330	1130	75	550	1187
MM2	1460	1510	690	2700	1284
MM3	-	1370	-	780	301

Note. — Masses are in $M_{\odot}$.

Table 7: Core Parameters at Peak Positions

Core	Transition	τ_ν	N[a] (cm^{-2})	$N(H_2)$ (cm^{-2})
MM1	$C^{18}O(3 \rightarrow 2)$	0.04	2.3×10^{15}	8.5×10^{21}
	$^{13}CO(3 \rightarrow 2)$	0.30	1.7×10^{16}	
	$C^{34}S(2 \rightarrow 1)$	0.02	1.9×10^{13}	4.3×10^{22}
	$CS(2 \rightarrow 1)$	0.41	4.3×10^{14}	
MM2	$C^{18}O(3 \rightarrow 2)$	0.37	2.3×10^{16}	8.5×10^{22}
	$^{13}CO(3 \rightarrow 2)$	2.80	1.7×10^{17}	
	$C^{34}S(2 \rightarrow 1)$	0.03	3.5×10^{13}	8.0×10^{22}
	$CS(2 \rightarrow 1)$	0.69	8.0×10^{14}	

Note. — Velocity range for the MM1 core: 54.0–59.3 km s^{-1}.
Velocity range for the MM2 core: 53.5–59.2 km s^{-1}.

[a]Column density for each molecule.

Table 8. Derived Parameters of Molecular Outflows

Core	Lobe	M_{lobe} ($M_\odot$)	M_{hidden} ($M_\odot$)	M_{total} ($M_\odot$)	P^{min} ($M_\odot$ km s^{-1})	P^{max} ($M_\odot$ km s^{-1})	E_k^{min} ($M_\odot$ km^2 s^{-2})	E_k^{max} ($M_\odot$ km^2 s^{-2})
MM1	Blueshifted	3	3	6	2.8×10^1	1.1×10^2	9.2×10^1	9.2×10^2
	Redshifted	13	6	19	9.5×10^1	3.3×10^2	3.5×10^2	2.9×10^3
	Total	16	9	25	1.2×10^2	4.4×10^2	4.4×10^2	3.8×10^3
MM2	Blueshifted	15	21	36	1.8×10^2	5.5×10^2	6.4×10^2	4.2×10^3
	Redshifted	32	12	44	2.2×10^2	6.7×10^2	7.8×10^2	5.2×10^3
	Total	47	33	80	4.0×10^2	1.2×10^3	1.4×10^3	9.4×10^3
MM3	Blueshifted	10	14	24	6.8×10^1	3.5×10^2	1.8×10^2	2.5×10^3
	Redshifted	8	9	17	4.9×10^1	2.4×10^2	1.1×10^2	1.8×10^3
	Total	18	23	41	1.2×10^2	5.9×10^2	2.9×10^2	4.3×10^3